Molecular Cell

Article

Nonstructural Protein 1 of SARS-CoV-2 Is a Potent Pathogenicity Factor Redirecting Host Protein Synthesis Machinery toward Viral RNA

Graphical Abstract

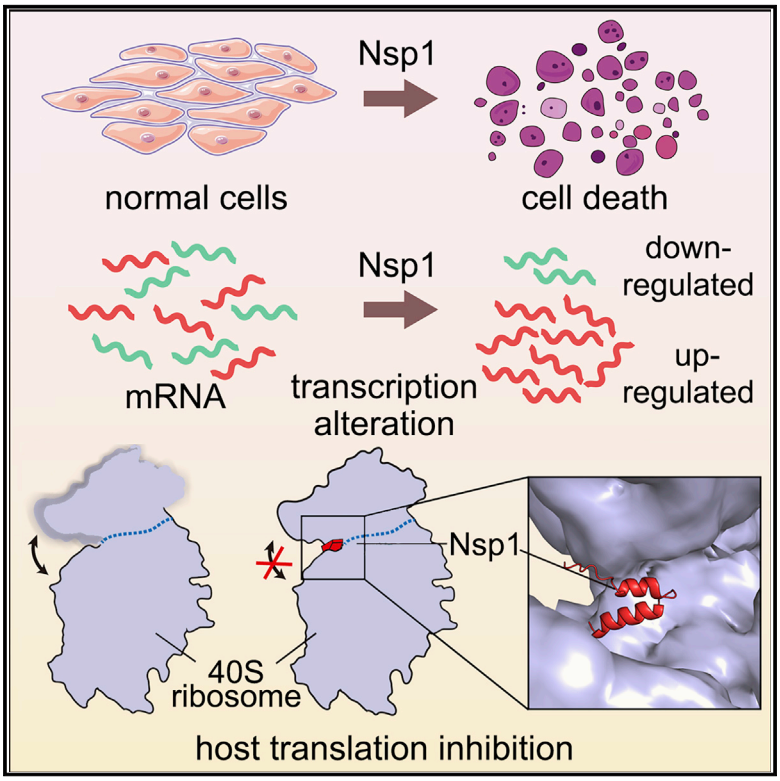

Highlights

- ORF screen identified Nsp1 as a major cellular pathogenicity factor of SARS-CoV-2
- Nsp1 broadly alters the gene expression programs in human cells of lung origin
- Nsp1 inhibits translation by blocking mRNA entry channel on the 40S ribosome
- Nsp1 prevents physiological conformation of the 48S preinitiation complex (PIC)

Authors

Shuai Yuan, Lei Peng, Jonathan J. Park, ..., Sidi Chen, Ivan B. Lomakin, Yong Xiong

Correspondence

sidi.chen@yale.edu (S.C.), ivan.lomakin@yale.edu (I.B.L.), yong.xiong@yale.edu (Y.X.)

In Brief

Yuan et al. used functional and cryo-EM studies to show that SARS-CoV-2 Nsp1 significantly reduces cell viability, induces extensive transcriptome alteration, and blocks host mRNA access to the ribosome. These results help understand how Nsp1 suppresses host gene expression and its broad impact as a comorbidity-inducing factor.

Yuan et al., 2020, Molecular Cell *80*, 1055–1066
December 17, 2020
https://doi.org/10.1016/j.molcel.2020.10.034

CellPress

Molecular Cell

CellPress

Article

Nonstructural Protein 1 of SARS-CoV-2 Is a Potent Pathogenicity Factor Redirecting Host Protein Synthesis Machinery toward Viral RNA

Shuai Yuan,[1,6] Lei Peng,[2,4,6] Jonathan J. Park,[2,4] Yingxia Hu,[1] Swapnil C. Devarkar,[1] Matthew B. Dong,[2,4] Qi Shen,[1] Shenping Wu,[5] Sidi Chen,[2,4,*] Ivan B. Lomakin,[3,*] and Yong Xiong[1,7,*]

[1]Department of Molecular Biophysics and Biochemistry, Yale University, New Haven, CT 06511, USA
[2]Department of Genetics, Yale University School of Medicine, New Haven, CT 06520, USA
[3]Department of Dermatology, Yale University School of Medicine, New Haven, CT 06520, USA
[4]Systems Biology Institute, Yale University, West Haven, CT 06516, USA
[5]Department of Pharmacology, Yale University, West Haven, CT 06516, USA
[6]These authors contributed equally
[7]Lead Contact
*Correspondence: sidi.chen@yale.edu (S.C.), ivan.lomakin@yale.edu (I.B.L.), yong.xiong@yale.edu (Y.X.)
https://doi.org/10.1016/j.molcel.2020.10.034

SUMMARY

The causative virus of the COVID-19 pandemic, SARS-CoV-2, uses its nonstructural protein 1 (Nsp1) to suppress cellular, but not viral, protein synthesis through yet unknown mechanisms. We show here that among all viral proteins, Nsp1 has the largest impact on host viability in the cells of human lung origin. Differential expression analysis of mRNA-seq data revealed that Nsp1 broadly alters the cellular transcriptome. Our cryo-EM structure of the Nsp1-40S ribosome complex shows that Nsp1 inhibits translation by plugging the mRNA entry channel of the 40S. We also determined the structure of the 48S preinitiation complex formed by Nsp1, 40S, and the cricket paralysis virus internal ribosome entry site (IRES) RNA, which shows that it is nonfunctional because of the incorrect position of the mRNA 3′ region. Our results elucidate the mechanism of host translation inhibition by SARS-CoV-2 and advance understanding of the impacts from a major pathogenicity factor of SARS-CoV-2.

INTRODUCTION

SARS-CoV-2, which causes the worldwide coronavirus disease 2019 (COVID-19) pandemic affecting millions of people, belongs to the β-coronaviruses (Coronaviridae Study Group of the International Committee on Taxonomy of Viruses, 2020). The virus contains a positive-sense and single-stranded RNA that is composed of 5′ UTR, two large overlapping open reading frames (ORF1a and ORF1b), structural and accessory protein genes, and a 3′-poly-adenylated tail (Lim et al., 2016). Upon entering the host cells, ORF1a and ORF1b are translated and proteolytically processed by virus-encoded proteinases to produce functional nonstructural proteins (Nsps) that play important roles in viral infection and RNA genome replication (Masters, 2006). Nsp1 is the first viral gene encoded by ORF1a (Figure 1A) and is among the first proteins to be expressed after infection (Ziebuhr, 2005). It was shown that human severe acute respiratory syndrome coronavirus (SARS-CoV) and group 2 bat coronavirus Nsp1 play a key role in suppressing the host gene expression (Kamitani et al., 2006; Narayanan et al., 2008; Tohya et al., 2009). SARS-CoV Nsp1 has been shown to inhibit host gene expression using a two-pronged strategy. Nsp1 targets the 40S ribosomal subunit to stall the translation in multiple steps during initiation of translation and also induces an endonucleolytic cleavage of host RNA to accelerate degradation (Kamitani et al., 2009; Lokugamage et al., 2012). Nsp1 therefore has profound inhibitory effects on the host protein production, including suppressing the innate immune system to facilitate the viral replication (Narayanan et al., 2008) and potentially long-term cell viability consequences. Intriguingly, viral mRNA overcomes this inhibition by a yet unknown mechanism, likely mediated by the conserved 5′ UTR of viral mRNA (Huang et al., 2011; Tanaka et al., 2012). Taken together, Nsp1 acts as an important factor in viral life cycle and immune evasion and may be an important virulence factor causing the myriad long-term illnesses of COVID-19 patients. It has been proposed as a target for live attenuated vaccine development (Wathelet et al., 2007; Züst et al., 2007).

It is common for RNA viruses to target the initiation step of the host protein translation system to allow expression of the viral proteins (Jan et al., 2016). Most cellular mRNAs have a 5′ 7-methylguanosine (m7G) cap structure, which is essential for

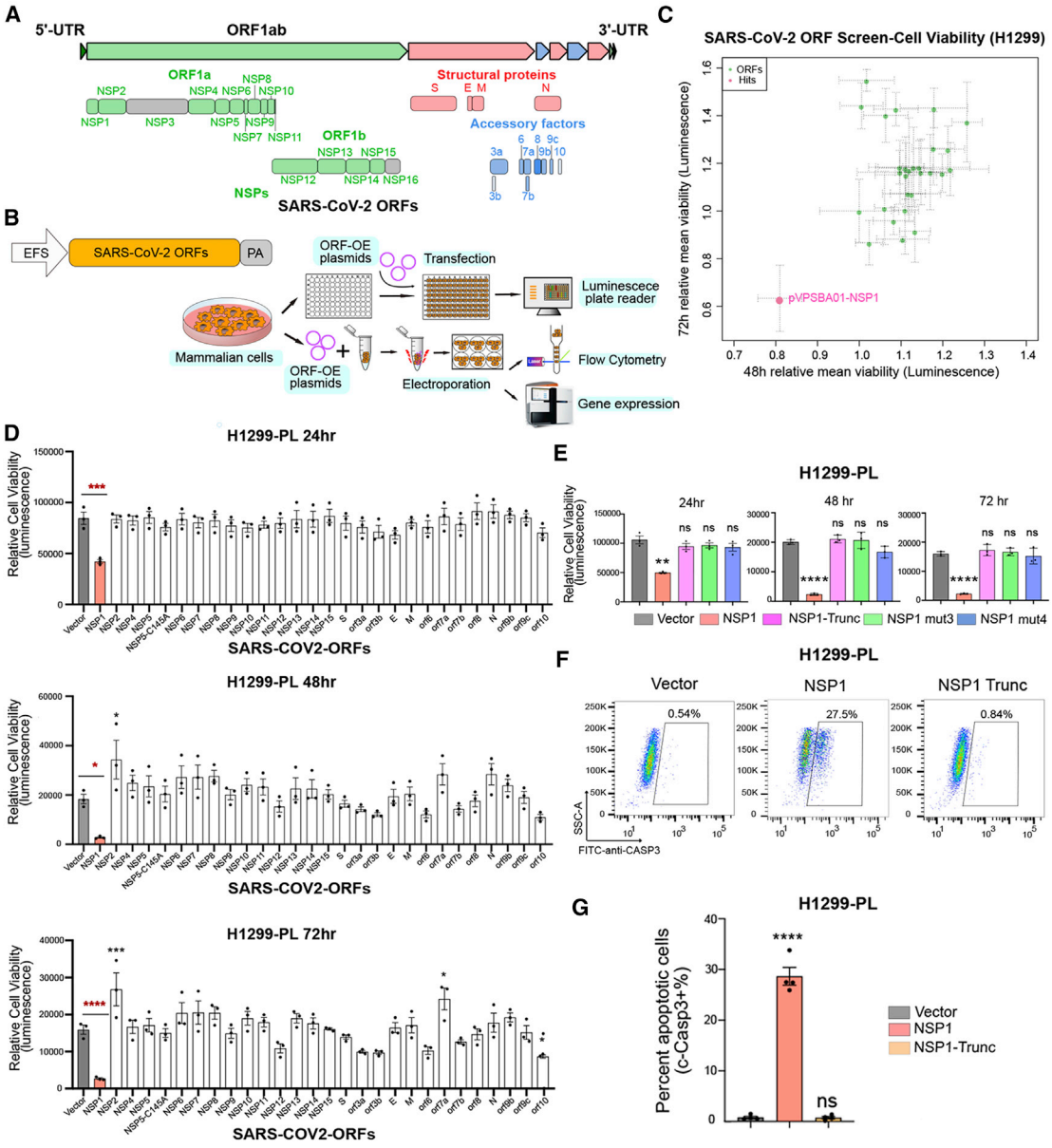

Figure 1. SARS-CoV-2 ORF Mini-screen Identified Nsp1 as a Key Viral Protein with Host Cell Viability Effect

(A) Schematics of viral protein coding frames along SARS-CoV-2 genome. Colored ORFs indicate the ones used in this study, while two ORFs in gray are not (Nsp3 and Nsp16).

(B) Schematics of molecular and cellular experiments of viral proteins.

(C) Scatterplot of SARS-CoV-2 ORF mini-screen for host viability effect in H1299 cells, at 48 and 72 h post-ORF introduction. Each dot represents the mean normalized relative viability of host cells transfected with a viral protein encoding ORF. Dashed-line error bars indicate SDs (n = 3 replicates). Pink color indicates hits with $p < 0.05$ (one-way ANOVA, with multiple-group comparison).

(D) Bar plot of firefly luciferase reporter measurement of viability effects of SARS-CoV-2 ORFs in H1299-PL cells, at 24, 48, and 72 h post-ORF introduction (n = 3 replicates).

(E) Bar plot of firefly luciferase reporter measurement of viability effects of Nsp1 and three Nsp1 mutants (truncation, mut3: R124S/K125E and mut4: N128S/K129E) in H1299-PL cells, at 24, 48, and 72 h post-ORF introduction (left, middle, and right panels, respectively) (n = 3 replicates).

(F) Flow cytometry plots of apoptosis analysis of Nsp1 and loss-of-function truncation mutant in H1299-PL cells, at 48 h post-ORF introduction. Percentage of apoptotic cells was gated as cleaved caspase-3-positive cells.

(G) Quantification of flow-based apoptosis analysis of Nsp1 and loss-of-function truncation mutant in H1299-PL cells, at 48 h post-ORF introduction.

For all bar plots in this figure, bar height represents mean value and error bars indicate standard error of the mean (SEM) (n = 3 replicates for each group). Statistical significance was accessed using ordinary one-way ANOVA, with multiple-group comparisons where each group was compared with empty vector control, with p values subjected to multiple-testing correction by FDR method (ns, not significant; *$p < 0.05$, **$p < 0.01$, ***$p < 0.001$, and ****$p < 0.0001$). See also Figure S1.

mRNA recruitment to the 43S preinitiation complex (PIC) through interaction with the translation initiation factor (eIF) eIF4F. 43S PIC is formed by the 40S ribosomal subunit, the ternary complex eIF2-GTP-Met-tRNA$_i^{Met}$, and the multi-subunit initiation factor eIF3. Binding of the 43S PIC to the m7G cap results in the loading of the mRNA in the mRNA-binding channel of the 40S to form the 48S PIC, and scanning of the mRNA from 5′ to 3′ direction under control of eIF1A and eIF1, until the initiation codon AUG is placed in the P site of the 40S. Base pairing of Met-tRNA$_i^{Met}$ with AUG results in conformational changes in the 48S PIC for joining the large 60S ribosomal subunit to form the 80S ribosome primed for protein synthesis (Hinnebusch, 2014, 2017; Hinnebusch et al., 2016). With the exception of type IV internal ribosome entry sites (IRESes), such as the cricket paralysis virus (CrPV) and Taura syndrome virus (TSV) IRESes, which do not require any host's eIFs, all other viruses may target different eIFs to redirect the host translational machinery on to their own mRNA (Hertz and Thompson, 2011; Lozano and Martínez-Salas, 2015; Walsh and Mohr, 2011).

We present here data demonstrating that among all viral proteins, Nsp1 causes the most severe viability reduction in the cells of human lung origin. The introduction of Nsp1 in human cells broadly alter the transcriptomes by repressing major gene clusters responsible for protein synthesis, mitochondria function, cell cycle, and antigen presentation, while inducing a broad range of factors implicated in transcriptional regulation. We further determined the cryoelectron microscopy (cryo-EM) structures of the Nsp1-40S complex with or without the CrPV IRES RNA, which reveal the mechanism by which Nsp1 inhibits protein synthesis and regulates viral protein production. These results significantly advance our understanding of the Nsp1-induced suppression of host gene expression, the potential mechanisms of SARS-CoV-2 translation initiation, and the broad impact of Nsp1 as a comorbidity-inducing factor.

RESULTS

SARS-CoV-2 ORF Screen Identifies Nsp1 as a Major Viral Factor that Affects Cellular Viability

In a recent study Gordon et al. (2020) mapped the interactome of viral protein to host cellular components in human HEK293 cells, suggesting that these viral proteins might have diverse ways of interacting or interfering with the fundamental cellular machineries of the host cell. We generated a non-viral overexpression vector (pVPSB) for introduction of viral proteins into mammalian cells and testing their effect on cells (Figure 1B). We first confirmed that the positive control GFP can be introduced into virtually all cells at 100% efficiency, using flow cytometry analysis. We cloned 28 viral proteins (27 of the 29 viral proteins and Nsp5 C145A mutation) as ORFs into this vector and introduced them into human cells by transfection. Intact cDNAs of Nsp3 and Nsp16 were not available when we performed the screen and thus were not included in the screen, therefore the cellular phenotypes of these two viral proteins have not been tested here. We chose to first test H1299, an immortalized cancer cell line of human lung origin. Although H1299 cells are not primary lung epithelial cells, they have been used as a cellular model to study SARS-CoV, MERS, and SARS-CoV-2 (Hoffmann et al., 2020; Wong et al., 2015).

We introduced all 28 cloned ORFs individually in parallel to conduct a mini-screen of viral proteins' effect on the viability of H1299 cells (Figures 1B and 1C). We measured cell viability at two time points, 48 and 72 h, post-transfection. Unexpectedly, we found Nsp1 as the sole "hit" with significant effect on cell viability at both time points (Figure 1C). To validate the viability observations with increased sensitivity, we generated an H1299 cell line with a constitutive firefly luciferase reporter (H1299-PL) and confirmed that GFP can also be introduced into this cell line at near 100% efficiency (Figures S1A–S1C). We performed validation experiments, again with all 28 ORFs along with vector control, at three different time points (24, 48, and 72 h). Across all three time points, Nsp1-transfected H1299 cells have dramatically reduced luciferase signal, an approximation of cell numbers (Figure 1D). We further repeat the same experiments with the Vero E6 cell line, an African monkey (*Cercopithecus aethiops*) kidney-derived cell line, commonly used in SARS-CoV-2 cellular studies (Blanco-Melo et al., 2020; Hoffmann et al., 2020; Kim et al., 2020; Zhou et al., 2020). Consistently, we observed a robust reduction of cellular viability in Vero E6 cells transfected with Nsp1 across all three time points (Figure S1D). These data revealed that among all SARS-CoV-2 proteins, Nsp1 has the largest detrimental effect on cell viability in H1299 and Vero E6 cells.

Nsp1 Mutants Abolish Cellular Viability Phenotype

To ensure that the observed reduction of cell viability is indeed from expression of functional Nsp1, we tested three different mutants of Nsp1, including a truncation mutation after residues 12 (N-terminal mutant, N-trunc) and two double mutations that have been reported to ablate the activity of SARS-CoV Nsp1 (Wathelet et al., 2007). As SARS-CoV Nsp1 is highly homologous to SARS-CoV-2 Nsp1, we hypothesize that these evolutionarily conserved amino acids may also have significant influence on the activity of SARS-CoV-2 Nsp1. The point mutations include Nsp1 mutant3, which has R124/K125 replaced with S124/E125 (R124S/K125E), and Nsp1 mutant4, which has N128/ K129 replaced with S128/E129 (N128S/K129E). We performed cellular viability assays with wild-type (WT) Nsp1 along with all three of its mutants. In both H1299-PL and Vero E6-PL cells, we again observed that introduction of Nsp1 into cells significantly reduced cell viability along 24, 48, and 72 h post-electroporation (Figures 1E and S1E). Each of the three mutants (truncation, R124S/K125E, and N128S/K129E) reverted this phenotype to the vector control level, fully abolishing the cytotoxic effect of Nsp1 (Figures 1E and S1E). These results confirmed that functional Nsp1, but not its loss-of-function mutants, induce reduction of cellular viability when overexpressed in the two mammalian cell lines.

We further tested if Nsp1 expression also leads to cell death. We introduced Nsp1 into H1299 cells, along with controls of empty vector and several other viral proteins (Nsp2, Nsp12, Nsp13, Nsp14, ORF9b, and Spike), and measured cellular apoptosis at 48 h post-electroporation by flow cytometry analysis of cleaved caspase-3 staining. We found that introduction of Nsp1, but not other viral proteins, induced apoptosis in

H1299 cells (Figure S1G). To ensure that the cellular apoptosis effect is indeed from the expression of functional Nsp1 protein, we performed the same apoptosis assay with Nsp1 and the three nonfunctional mutants described above. Consistently, only WT Nsp1 induced apoptosis in H1299-PL cells, whereas the three mutants did not (Figure S1F). Replicates of this cleaved caspase-3 flow assay with the truncation mutation of Nsp1 confirmed that WT Nsp1, but not the loss-of-function truncation mutant, induced apoptosis in H1299-PL cells (Figures 1F and 1G).

Transcriptome Profiling of Nsp1-Overexpressed Cells

To unbiasedly investigate the global gene expression changes induced by Nsp1 or its loss-of-function mutant form, we performed transcriptome profiling. We first confirmed that Nsp1 is indeed overexpressed in host cells by qPCR using a custom-designed NSP1-specific probe, at both 24 and 48 h post-electroporation (Figure 2A). We then electroporated in quadruplicate for each of Nsp1, its truncation mutant, or vector control plasmid into H1299-PL cells and collected samples 24 h post-electroporation for mRNA sequencing (mRNA-seq). We collected 24 h instead of 48 or 72 h samples in order to capture the earlier effect of Nsp1 on cellular transcriptome. We mapped the mRNA-seq reads to the human transcriptome and quantified the expression levels of annotated human transcripts and genes (Table S3). Principal-component analysis showed clear grouping and separation of WT Nsp1, mutant Nsp1, and vector control groups (Figure 2B), confirming the overall quality of the Nsp1 mRNA-seq dataset.

Differential expression analysis revealed broad and potent gene expression program changes induced by Nsp1 (Figure 2C; Tables S3 and S4), with 5,394 genes significantly downregulated and 3,868 genes significantly upregulated (false discovery rate [FDR]-adjusted $q < 0.01$). To examine the highly differentially expressed genes, we used a highly stringent criteria (FDR-adjusted $q < 1e\text{-}30$) and identified 1,245 highly significantly downregulated genes (top NSP1-repressed genes) and 464 highly significantly upregulated genes (top Nsp1-induced genes) (Figure 2C; Tables S3 and S4). In sharp contrast, Nsp1 truncation mutant and the vector control showed no differential expression in the transcriptome, even when using the least stringent criteria (FDR-adjusted $q < 0.05$) (Figures S2A and S2B; Tables S3 and S4). These data revealed that Nsp1 alone can cause major alterations broadly in the transcriptome shortly (24 h) after its introduction into host cells, consistent with its cell viability phenotype (Figure 1).

Enriched Pathway Analysis on Differentially Expressed Gene Sets Revealed Strong Signatures of Cellular Transcriptome Alterations by Nsp1

We globally examined the highly differentially expressed genes as a result of Nsp1 expression. To understand what these genes represent as a group, we performed DAVID clustering and biological processes (BP) analysis on the 1,245 top Nsp1-repressed genes and the 464 top Nsp1-induced genes, respectively (Figure 2D; Table S4). Enriched pathways in the top Nsp1-repressed genes showed that the most significant Gene Ontology groups include functional annotation clusters of ribosomal proteins and translation related processes, such as terms of ribonucleoprotein (RNP) (hypergeometric test, FDR-adjusted q = 6.30e-57), ribosomal RNA processing (q = 2.03e-28), and translation (q = 3.93e-28). Highly enriched Nsp1-repressed genes also include the clusters of mitochondria function and metabolism (most terms with $q < 1e\text{-}15$) and cell cycle and cell division (most terms with $q < 1e\text{-}10$), consistent with the reduced cell viability phenotype. Other intriguing enriched Nsp1-repressed pathways include ubiquitin/proteasome pathways and antigen-presentation activities, as well as mRNA processing. We further performed gene set enrichment analysis (GSEA), which takes into consideration both gene set and ranks of enrichment, and the results largely validated the DAVID findings, with highly similar strongly enriched pathways (Figures 3A and S2C). Analysis of highly differentially expressed genes between Nsp1 and Nsp1 mutant showed results virtually identical to those of Nsp1 versus vector (Figures S2A and S2B; Table S4).

We then examined the expression levels of the highly differentially expressed genes in the context of enriched pathways in Nsp1, mutant Nsp1, or vector control plasmid in H1299-PL cells. As shown in the heatmaps (Figure 3B), more than 70 genes involved in translation are strongly repressed upon introduction of Nsp1, including the RPS, RPL, MRPS, and MRPL family members, along with other translational regulators, such as *AKT1*. The repression effect on these genes is completely absent in the Nsp1 mutant group (Figure 3B). The strong repression effect also hit multiple members of the gene families involved in mitochondria function, such as the COX, NUDFA, NUDFB, and NUDFS families (Figure 3C). Consistent with the cellular phenotypes, Nsp1 also repressed a large number of mitotic cell cycle genes, including members in the CDK, CDC, and CCNB families, components of the centrosome, the anaphase-promoting complex, and various kinases (Figure 3D). Although part of the signal may be driven by ribosomal and/or proteasomal genes, multiple genes involved in the mRNA processing and/or nonsense-mediated decay nevertheless are significantly repressed by Nsp1 (Figures S2D and S2E). Interestingly, DAVID BP enrichment analysis of Nsp1-repressed genes also scored the antigen presentation pathway, mostly proteasome components along with several MHC-I component members (Figure 3E). Concordantly, Nsp1-repressed genes are also enriched in the ubiquitination and proteasome degradation pathways (Figure S2F).

On the other hand, genes highly induced by Nsp1 hit a broad range of factors implicated in transcriptional regulation, such as unfolded protein response regulators (*ATF4*, *XBP1*), FOX family transcription factors (TFs) (*FOXK2*, *FOXE1*, *FOXO1*, *FOXO3*), zinc finger protein genes (*ZFN217*, *ZFN567*), KLF family members (*KLF2*, *KLF10*), SOX family members (*SOX2*, *SOX4*), homeobox genes (*HOXD9*, *HOXC8*, *HOXD13*), GATA TFs (*GATAD2B*, *GATA6*), dead-box protein genes (*DDX5*, *DHX36*), and cell fate regulators (*RUNX2*, *CREBRF*, *LIF*, *JUNB*, *ELK1*, *JAG1*, *SMAD7*, *BCL3*, *EOMES*), along with certain epigenetic regulators of gene expression such as the SWI/SNF family members *ARID1A*, *ARID1B*, *ARID3B*, and *ARID5B* (Figure 3F). Interestingly, highly upregulated genes are also slightly enriched in the MAPK/ERK pathway, where Nsp1 expression induces multiple DUSP family members (Figure 3G). The upregulated genes also include several KLF family members related to the process of cellular response to peptide (Figure S2G). Again, the induction

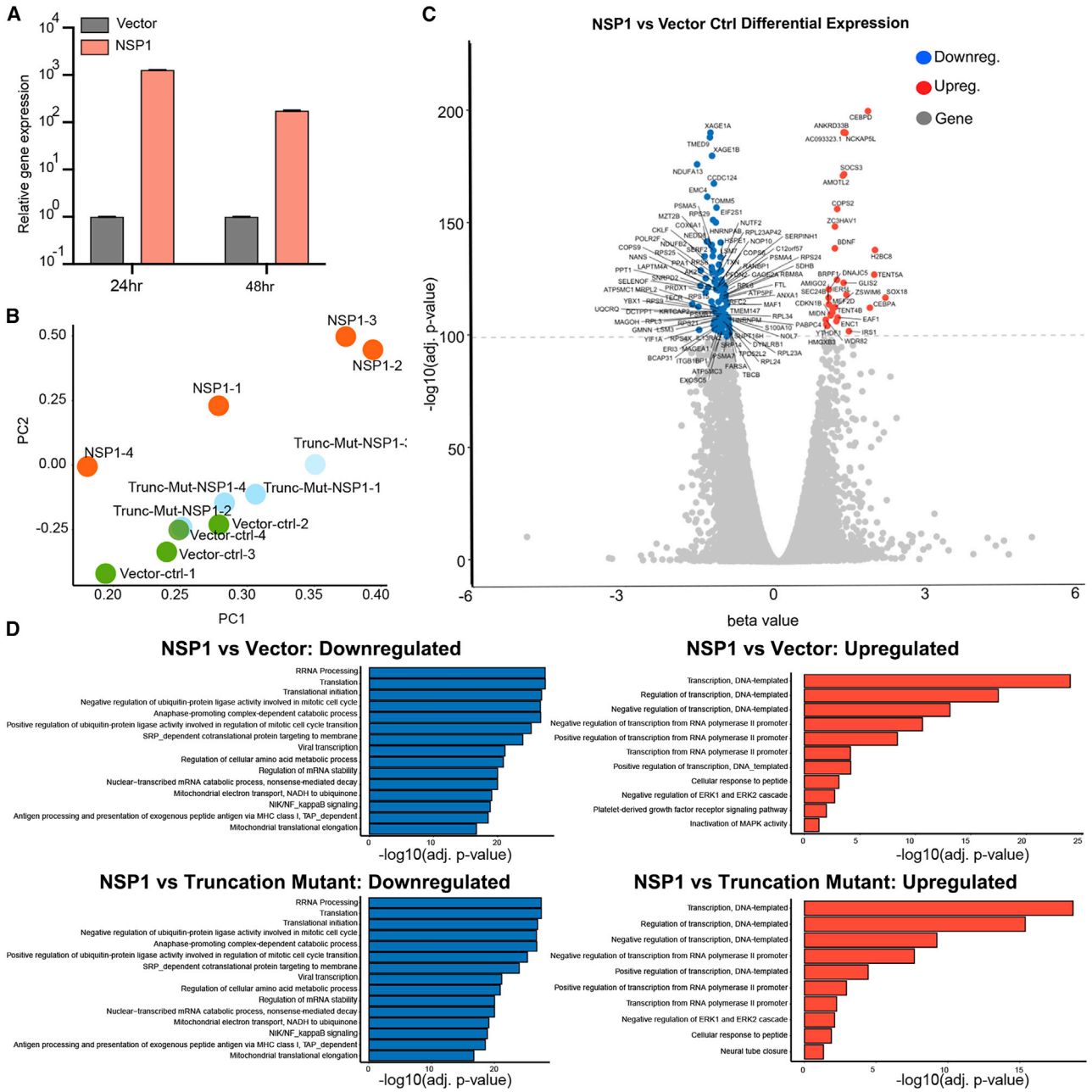

Figure 2. Transcriptome Profiling of H1299 Cells Introduced with NSP1 and NSP1 Truncation Mutant by RNA-Seq

(A) Quantitative PCR (qPCR) confirmation of *NSP1* overexpression, at 24 and 48 h post-electroporation (n = 3 replicates).

(B) Principal-component analysis (PCA) plot of the entire mRNA-seq dataset, showing separation between Nsp1, vector control, and Nsp1 truncation mutant groups, all electroporated into H1299-PL cells and harvested 24 h post-electroporation. RNA samples were collected as quadruplicates (n = 4 each group).

(C) Volcano plot of differential expression between of Nsp1 versus vector control electroporated cells. Top differentially expressed genes (FDR-adjusted q < 1e-100) are shown with gene names. Upregulated genes are shown in orange. Downregulated genes are shown in blue.

(D) Bar plot of top enriched pathway analysis by DAVID biological processes (BP). Nsp1 versus vector control (top) or Nsp1 versus Nsp1 mutant (bottom); highly downregulated (left) and upregulated (right) genes are shown (q < 1e-30).

See also Figure S2.

effect on these genes is completely abolished in the Nsp1 mutant group (Figures 3F and 3G). These data together showed that Nsp1 expression broadly and significantly altered multiple gene expression programs in the host H1299-PL cells.

Cryo-EM Structure Reveals Nsp1 Is Poised to Block Host mRNA Translation

To elucidate the mechanism of translation inhibition by Nsp1, we determined the cryo-EM structure of rabbit 40S ribosomal

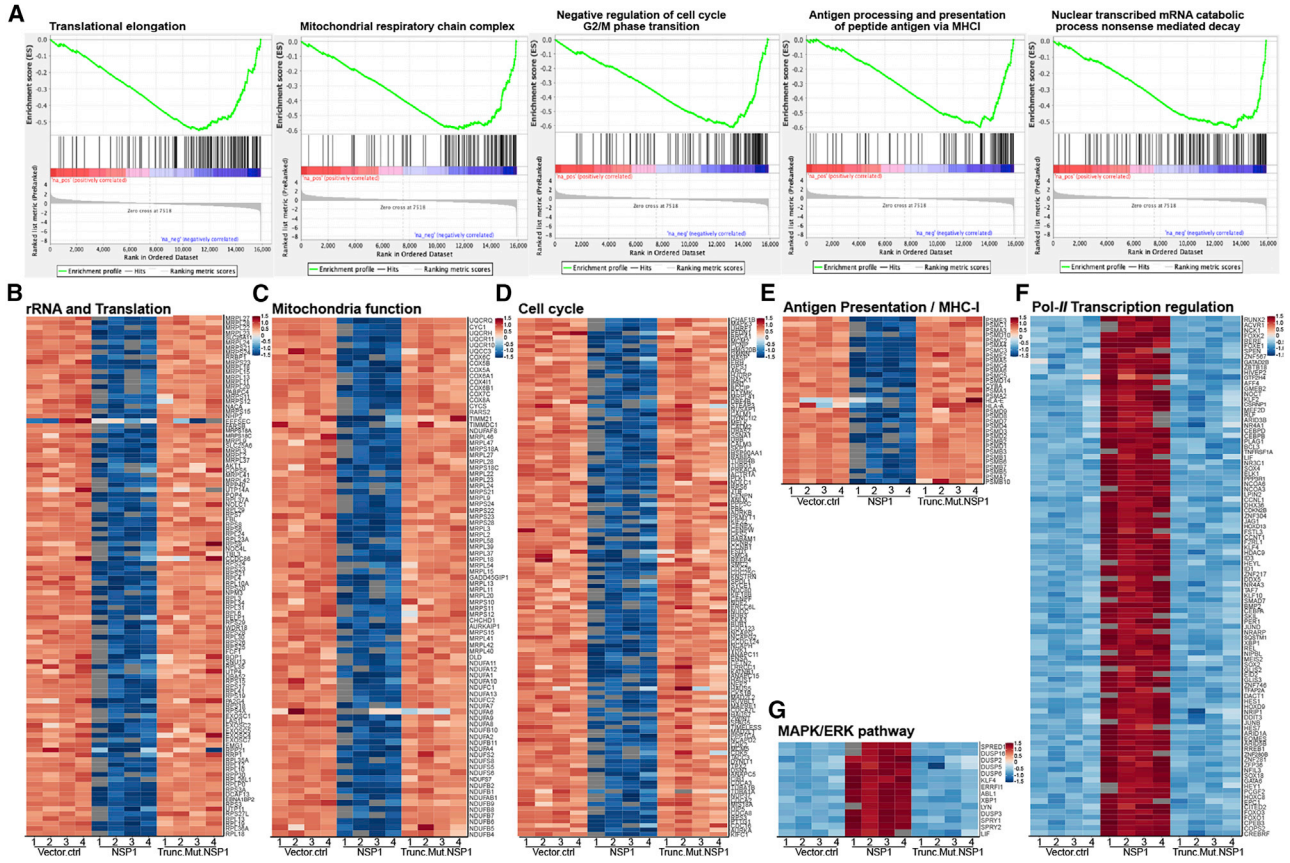

Figure 3. Highly Differentially Expressed Genes between Nsp1, Vector Control, and Nsp1 Mutant Group in the Context of Top Major Enriched Pathways

(A) Gene set enrichment plots of representative enriched pathways by GSEA.

(B–E) Heatmap of Nsp1 highly repressed genes (q < 1e-30) in rRNA processing and translation (B), mitochondria function (C), cell cycle (D), and MHC-I antigen presentation processes (E).

(F and G) Heatmap of Nsp1 highly induced genes (q < 1e-30) in *polII*-related transcription regulation processes (F) and the MAPK/ERK pathway (G).

See also Figure S2.

subunit complex with Nsp1 at 2.7 Å resolution (Table 1; Figure S3). The density observed in the mRNA entry channel enabled us to build an atomic model for the C-terminal domain of Nsp1 (C-Nsp1, amino acids [aa] 145–180) (Figure 4A). C-Nsp1 comprises two α helices (α1, aa 154–160; α2, aa 166–179) and two short loops (aa 145–153 and 161–165), which block the mRNA entry channel (Figures 4A and 4B). Besides the α helices in the mRNA channel, extra globular density between the ribosomal protein uS3 and rRNA helix h16 is observed at a lower contour level, whose dimensions roughly matched the N-terminal domain of Nsp1 (aa 13–127, N-Nsp1, PDB: 2HSX) (Almeida et al., 2007) (Figure 4C). However, N-Nsp1 does not appear to be stably bound to the 40S, and the low local resolution of the cryo-EM map in this region did not allow an atomic model for the N-Nsp1.

C-Nsp1 bridges the head and body domains of the 40S ribosomal subunit through extensive electrostatic and hydrophobic interactions with the ribosomal proteins uS3 of the head, uS5 and eS30, and helix h18 of the 18S rRNA in the body (Figure 4D). The negatively charged residues D152, E155, and E159 of C-Nsp1 interact with the positively charged residues R117, R116, R143, and K148 of uS3, respectively (Figure 4E). In addition, K164 and H165 of Nsp1 inserts into the negatively charged pocket formed by the backbone of U607, G625, and U630 of the rRNA h18. R171 and R175 of C-Nsp1 interact with the negatively charged patch formed by G601, A604, G606, and U607 of h18 (Figure 4E). Besides electrostatic contacts, a large hydrophobic patch of C-Nsp1, which is formed by F157, W161, L173, and L177, interacts with a complementary hydrophobic patch on uS5 formed by V106, I109, P111, T122, F124, V147, and I151 (Figure 4E). Intriguingly, K164 and H165 of Nsp1, which have been shown to play an important role in host translation inhibition, are conserved only in the betacoronaviruses (beta-CoVs) (Figure S4). In addition, the other Nsp1 residues interacting with the h18 of rRNA are also conserved only among the beta-CoVs (Figure S4). This sequence conservation indicates that the hydrophobic interactions between C-Nsp1 and uS5 are likely universal in both alpha- and beta-CoVs, while the electrostatic

Table 1. Cryo-EM Data Collection, Refinement, and Validation Statistics

	Nsp1-40S Ribosome (EMDB-22432) (PDB: 7JQB)	Nsp1-40S-CrPV IRES (EMDB-22433) (PDB: 7JQC)
Data Collection and Processing		
Magnification	81,000	81,000
Voltage (kV)	300	300
Electron exposure (e–/Å^2)	50	50
Defocus range (μm)	0.5–2.0	0.5–2.0
Pixel size (Å)	1.068	1.068
Symmetry imposed	C1	C1
Initial particle images (no.)	668,695	60,690
Final particle images (no.)	353,927	48,689
Map resolution (Å)	2.7	3.3
FSC threshold	0.143	0.143
Map resolution range (Å)	2.5–4.5	3.0–5.0
Refinement		
Initial model used (PDB code)	4KZX	4KZX
Model resolution (Å)	2.7	3.3
FSC threshold	0.143	0.143
Model Resolution Range (Å)		
Map sharpening *B* factor (Å^2)	88	23
Model Composition		
Non-hydrogen atoms	74,976	77,833
Protein residues	4,859	4,837
Ligands (nucleotide)	1,697	1,840
B Factors (Å^2)		
Protein	140	140
Ligand (nucleotide)	150	167
RMSDs		
Bond lengths (Å)	0.007	0.006
Bond angles (°)	0.8	0.9
Validation		
MolProbity score	1.8	1.9
Clashscore	6.4	7.9
Poor rotamers (%)	0.4	0.5
Ramachandran Plot		
Favored (%)	93.03	92.28
Allowed (%)	6.91	7.55
Disallowed (%)	0.06	0.17

See also Figures S3 and S6.

interactions between C-Nsp1 and the h18 of the 18S rRNA are conserved only in the beta-CoVs. The extensive interactions result in C-Nsp1 plugging the mRNA entry channel, which prevents the loading and accommodation of the mRNA (Figure 4B), providing a structural basis for the inhibition of host protein synthesis by Nsp1 of SARS-CoV-2 and SARS-CoV reported previously (Kamitani et al., 2006, 2009).

Nsp1 Locks the 40S in a Conformation Incompatible with mRNA Loading and Disrupts Initiation Factor Binding

The ribosomal protein uS3 is conserved in all kingdoms. Together with h16, h18, and h34 of 18S rRNA it constitutes the mRNA-binding channel and the mRNA entry site (Graifer et al., 2014; Hinnebusch, 2017). It has been shown that uS3 interacts with the mRNA and regulates scanning-independent translation on a specific set of mRNAs (Haimov et al., 2017; Sharifulin et al., 2015). Interestingly, conserved residues R116 and R117 of uS3, which are crucial for stabilizing mRNA in the entry channel and maintaining 48S PIC in the closed conformation, are interacting with D152 and E155 of Nsp1 in our structure (Dong et al., 2017; Hinnebusch, 2017) (Figure 4E). Moreover, the conformation of the 40S ribosomal subunit in Nsp1-40S complex is similar to that of "closed state" of 48S PIC with initiator tRNA locked in the P site and the latch closed (Lomakin and Steitz, 2013), which is incapable of mRNA loading. The distance between G610 (h18) and GLN179 (CA, uS3) is shortened from 19.4 Å in the "open state" 48S PIC (PDB: 3JAQ) to 15.8 Å in Nsp1-40S ribosomal complex, which is similar to the distance of 15.0 Å in the closed state 48S PIC (PDB: 4KZZ) (Figure 4F). This shows that Nsp1 not only plugs the mRNA entry channel but also keeps the 40S subunit in a conformation that is incompatible with mRNA loading.

The known structure of the N-terminal domain of SARS-CoV (N-Nsp1) (Almeida et al., 2007) (PDB: 2HSX) can be docked into the extra globular density between uS3 and rRNA helix h16 in the cryo-EM map (Figure 4G). This potential interaction between N-Nsp1 and uS3 covers most of the uS3 surface on the solvent side, including the GEKG loop of uS3 (aa 60–63) that corresponds to the consensus GXXG loop conserved in the KH domains of various RNA-binding proteins (Babaylova et al., 2019; Graifer et al., 2014). Mutation of the GEKG loop to alanines does not abrogate the ability of the 40S to bind mRNA and form 48S PIC. Instead, it results in the formation of aberrant 48S PIC that cannot join the 60S ribosomal subunit and assemble the 80S initiation complex (Graifer et al., 2014). Peculiarly, binding of SARS-CoV Nsp1 to the ribosome led to the same effect (Kamitani et al., 2009). We hypothesize that Nsp1 may prevent the formation of physiological conformation of the 48S PIC induced by uS3 interaction with eIFs, such as the j subunit (eIF3j) of the multi-subunit initiation factor eIF3 (Babaylova et al., 2019; Cate, 2017; Sharifulin et al., 2016). The eIF3 complex plays a central role in the formation of the translation initiation complex (Cate, 2017; Hinnebusch, 2014). eIF3j alone binds to the 40S ribosomal subunit and stabilizes the interaction with eIF3 complex (Fraser et al., 2004; Sokabe and Fraser, 2014). The binding site of eIF3j to 40S subunit is not precisely determined. Cryo-EM and biochemical studies mapped it onto the mRNA-binding channel of the 40S, extending from the decoding center toward the mRNA entry region, including the GEKG loop of uS3 (Aylett et al., 2015; Fraser et al., 2007; Hershey, 2015) (Figure 4G).

We tested if Nsp1 can compete with eIF3j for the binding to the 40S ribosomal subunit. The result showed that Nsp1 indeed significantly reduces the binding between eIF3j and the 40S (Figure 4H). The binding competition of eIF3j and Nsp1 to the 40S was tested at different concentrations. There is little eIF3j binding to the 40S when the concentration of eIF3j is equal or lower than

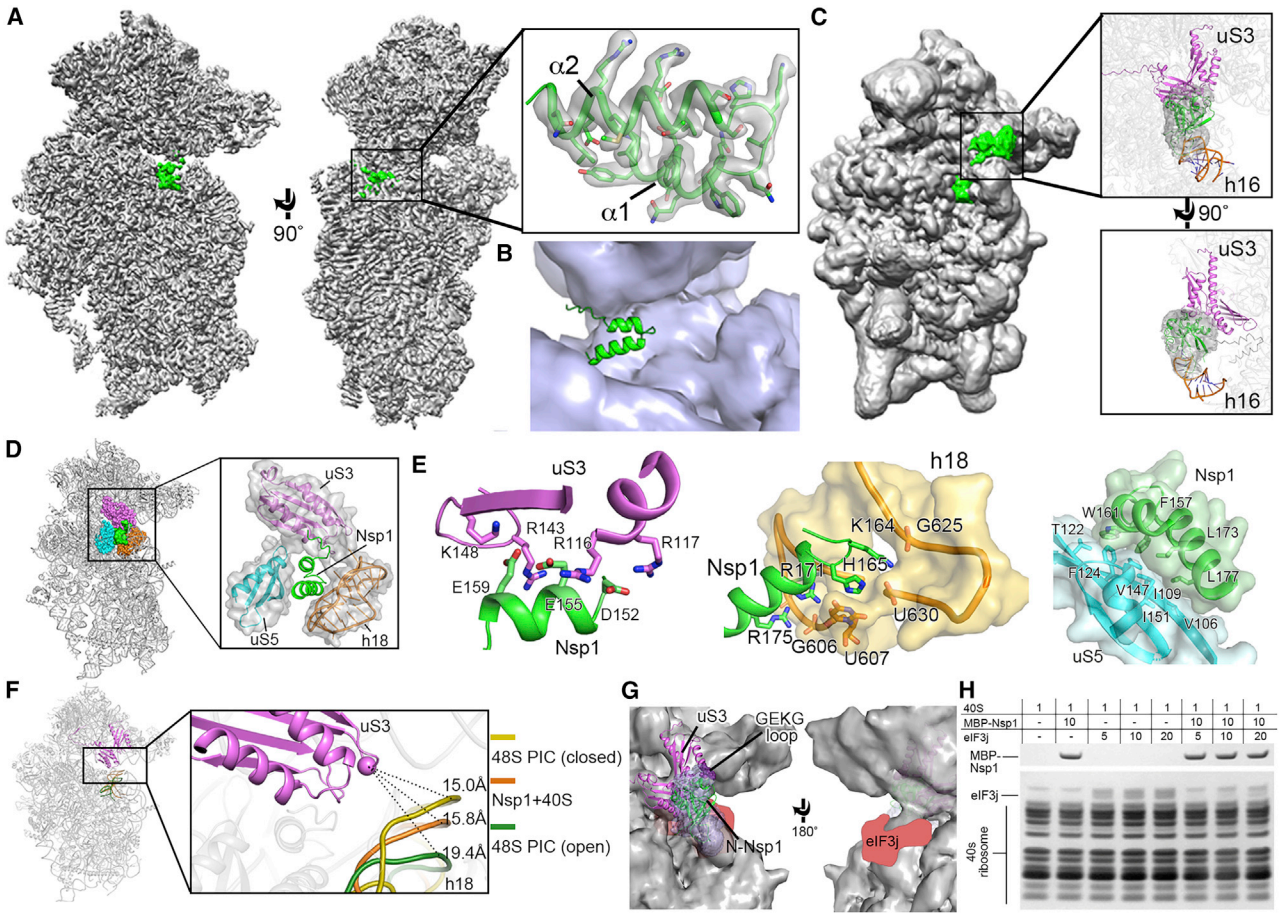

Figure 4. Cryo-EM Structure of the Nsp1-40S Ribosome Complex

(A) Overall density of the Nsp1-40S ribosome complex with Nsp1 (green) and 40S ribosome (gray). Inset shows C-Nsp1 with corresponding density with clear sidechain features. C-Nsp1 α helices (α1, aa 154–160; α2, aa 166–179) are labeled.

(B) Cross section of the C-Nsp1 (green) within the mRNA entry channel. 40S ribosome is shown in surface, and C-Nsp1 is displayed in cartoon.

(C) Overall density of Nsp1-40S ribosome complex at a lower contour level. Insets show the extra globular density with SARS-CoV Nsp1 N-terminal domain (PDB: 2HSX, green) fitted. Ribosomal protein uS3 (magenta) and rRNA h16 (orange) are shown in cartoon.

(D) Overall structure of the C-Nsp1-40S ribosome complex, with C-Nsp1 (green surface) and the surrounding protein uS3 (magenta sphere representation), uS5 (cyan) and rRNA h18 (orange) highlighted. The inset shows zoomed-in view of C-Nsp1 in cartoon, with the surrounding 40S components in cartoon and surface to illustrate the mRNA entry channel.

(E) Molecular interactions between C-Nsp1 and 40S ribosome components, including uS3, h18, and uS5. Proteins and rRNA are in the same color as in (D) and shown in cartoon, with binding pocket and hydrophobic interface depicted in surface. The interacting residues are shown in sticks.

(F) The conformation of the 40S ribosome in the Nsp1-40S complex is similar to the close form in the 48S PIC. Q179 of uS3 (magenta cartoon) is displayed as a sphere. h18 is in cartoon and colored dark yellow (48S closed conformation), orange (Nsp1-40S ribosome complex), and dark green (48S open conformation), with distances to Q179 indicated by the dashes.

(G) The N-terminal domain of Nsp1 covers uS3 surface on the solvent side. The cryo-EM density in this region is shown in blue surface with SARS-CoV Nsp1 N-terminal domain (PDB: 2HSX) fitted. uS3 (magenta) is depicted in cartoon. The GEKG loop (dark purple) is shown in sphere representation. The putative location of eIF3j is marked in red.

(H) SDS-PAGE analysis of Nsp1 and eIF3j competition at different concentration ratios (indicated in the top table).

See also Figures S3–S5.

that of Nsp1, and residual eIF3j binding was observed only when its concentration is higher than that of Nsp1 (Figures 4H and S5). In contrast, the binding of Nsp1 to the 40S is not affected even when eIF3j is in excess. These results indicate that Nsp1 disrupts the binding of eIF3j to the 40S, potentially by shielding the access to uS3 and the mRNA-binding channel and/or by making the conformation of the 40S unfavorable for eIF3j interaction.

Nsp1 Prevents Physiological Conformation of the 48S PIC

It was shown previously that binding of SARS-CoV Nsp1 to the 40S ribosomal subunit does not inhibit 48S PIC formation, but it suppresses 60S subunit joining (Kamitani et al., 2009). To understand the effect of Nsp1 of SARS-CoV-2 on 48S PIC, we determined a 3.3 Å resolution cryo-EM structure of Nsp1 bound

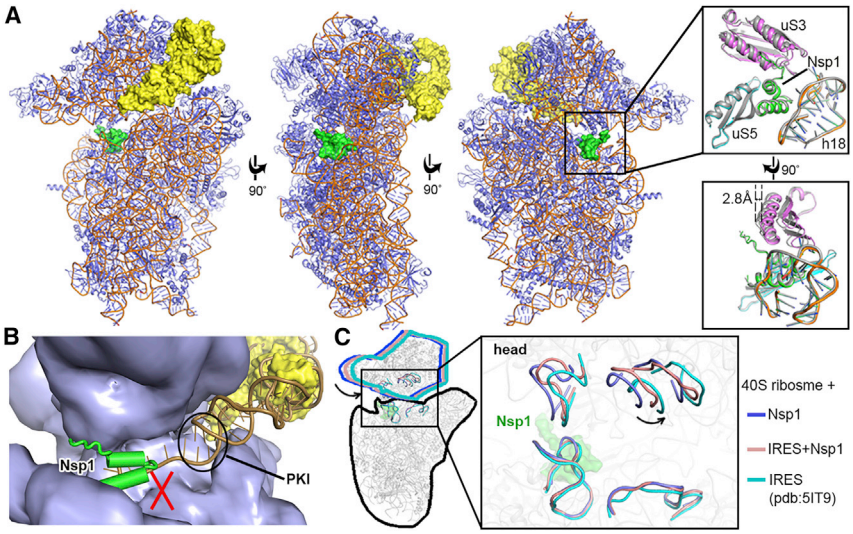

Figure 5. Nsp1 Prevents Physiological Conformation of the 48S PIC

(A) Overall structure of the Nsp1-40S-CrPV IRES complex. Nsp1 (green) and IRES (yellow) are presented in surface. The ribosome proteins (slate) and rRNA (orange) are shown in cartoon. The right insets display the conformation change in the Nsp1-binding region (cartoon representation) with or without the IRES.

(B) The previously reported model of CrPV IRES (PDB: 5IT9; orange cartoon) fitted to 40S ribosome in the present of Nsp1 (green cartoon). 40S ribosome (slate) and the currently observed IRES (yellow) are presented in surface.

(C) C-Nsp1 restricts the 40S ribosome head rotation. Superposition of the Nsp1-40S, Nsp1-40S-CrPV IRES, and IRES-40S (PDB: 5IT9) complexes is shown is cartoon. Zoomed view displays the head rotations represented by selected rRNA regions. C-Nsp1 (green) is displayed in surface.

See also Figure S6.

to the 48S PIC assembled with the CrPV IRES (Figures 5A and S6). CrPV IRES has become an important model for studies of the eukaryotic ribosome during initiation, as it is able to directly recruit and assemble with 40S or 80S ribosome without requiring any eIFs (Martinez-Salas et al., 2018). It was shown that SARS-CoV Nsp1 inhibits translation of the CrPV IRES RNA (Kamitani et al., 2009). The use of CrPV IRES allowed us to probe if Nsp1 completely inhibits mRNA binding to the 40S subunit or it acts on the mRNA entry site only, as binding of the IRES may help fix 5′ region of the mRNA on the ribosome mRNA exit region, enabling the investigation of the mRNA path on the 40S subunit in the presence of Nsp1. We first examined whether Nsp1 affects binding of the IRES RNA to the 40S ribosomal subunit. The result shows that Nsp1 and CrPV IRES can bind 40S ribosomal subunit simultaneously (Figures S6A and S6B). Consistently, both C-Nsp1 and the CrPV IRES can be seen in the cryo-EM map (Figure 5A), where the Nsp1 C-terminal domain is inserted in the RNA entry channel in the same way as in the Nsp1-40S complex without the IRES RNA (Figures 4A and 4B). The local environment of C-Nsp1 in the ribosome RNA entry channel with or without the IRES RNA is quite similar. No conformational changes were observed for C-Nsp1, protein uS5, and rRNA h18, but the head of the 40S subunit is moved by about 2.8 Å (Figure 5A) (discussed more below).

We fitted the high-resolution structure of the CrPV IRES from the yeast 40S-CrPV IRES complex (Murray et al., 2016) (PDB: 5IT9) into our cryo-EM map. Importantly, the pseudoknot I (PKI) domain of the CrPV IRES, which is a structural mimic of the canonical tRNA-mRNA interaction, is not seen in the cryo-EM map, suggesting that it is dislodged from the 40S in the presence of Nsp1 (Figure 5B). Consistently, there would be a clash between Nsp1 C-terminal domain and the 3′ region of the IRES RNA in the previously observed conformation bound to the 40S (Murray et al., 2016) (Figure 5B). The conformation of the 40S head in the Nsp1-40S-CrPV IRES complex is different from that in the Nsp1-40S complex (Figure 5C). The head in the Nsp1-40S-CrPV IRES complex is in somewhat intermediate conformation compared with the Nsp1-40S and the 40S-CrPV IRES complexes (Figure 5C). This suggests that the Nsp1-40S interactions resist the conformational changes induced by the IRES for translation initiation. Conformational changes of the head domain of the 40S subunit play important role in the mRNA loading and recruitment of the 60S subunit to form the 80S ribosome. Nsp1 limits the rotation of the head, which may have profound consequences interfering with the joining of the 60S subunit and the formation of the 80S initiation complex.

DISCUSSION

Viral infection is a complex process involving multiple components, and certain viral proteins are often in high abundance in cells during active viral replication (Astuti and Ysrafil, 2020; Yoshimoto, 2020). Therefore, understanding the effects of each individual viral protein on the cells provides important insights on the cellular impacts of viral infection. Using a reductionist approach, we tested the gross cellular effect of expressing most of the SARS-CoV-2 proteins individually and found that among all ORFs tested, Nsp1 showed the strongest deleterious effect on cell viability in H1299 cells of human lung epithelial origin. This is in concordance with previous observations from related coronaviruses, such as mouse hepatitis virus (MHV) Nsp1 being a major pathogenicity factor strongly reducing cellular gene expression (Züst et al., 2007), and SARS-CoV Nsp1 inhibiting interferon (IFN)-dependent signaling and having significant effects on the cell cycle (Wathelet et al., 2007). A recent study showed that SARS-CoV-2 Nsp1 shuts down mRNA translation in cells and suppresses innate immunity genes such as *IFNb* and *IL-8*, although these experiments were conducted in HEK293T cells of kidney origin, and only a small number of host genes were tested (Thoms et al., 2020a). As an unbiased interrogation of global cellular pathways affected by Nsp1, our transcriptome profiling data and GSEA revealed strong signatures of transcriptomic changes in broad ranges of host genes with several major clusters, providing a comprehensive understanding of the impacts of one of the most potent pathogenicity protein factors of SARS-CoV-2 in human cells of lung origin.

Our structure of the SARS-CoV-2 Nsp1 protein bound to the 40S ribosomal subunit establishes a mechanistic basis of the cellular effects of Nsp1, revealing a multifaceted mechanism of inhibition of the host protein synthesis at the initiation stage by the virus. Nsp1 plugs the mRNA channel entry, which physically blocks access to the channel by any mRNA (Figure 4B). Moreover, Nsp1 locks the head domain of the 40S subunit in the closed position, characterized by the closed conformation of the "mRNA entry channel latch" that clams around incoming mRNA (Hinnebusch, 2017; Lomakin and Steitz, 2013; Passmore et al., 2007). The latch is supposed to be closed during the scanning of the mRNA, keeping mRNA locked in the binding cleft and increasing processivity of the scanning, whereas the open conformation of the latch would facilitate the initial attachment of the 43S PIC to the mRNA (Lomakin and Steitz, 2013). Therefore, when Nsp1 keeps the latch closed, it makes it impossible for the host mRNA to be loaded. In addition, we showed that Nsp1 competes with eIF3j for the binding to the 40S subunit (Figure 4H). This allows us to propose that Nsp1 weakens the binding of the eIF3 to the 40S subunit by disrupting uS3-eIF3j interaction. Recently, several structures of Nsp1 bound ribosomal complexes were reported, including binary (Nsp1-40S), with ribosome biogenesis factor TSR1, and with eIF3-containing PICs (Schubert et al., 2020; Thoms et al., 2020a). None of these structures, however, captured the mRNA, which likely is flexible or dissociates from the PIC because of the lack of the mRNA-eIF4F interaction. Using CrPV IRES RNA, we were able to visualize the RNA bound to Nsp1-40S complex and show that Nsp1 does not inhibit mRNA binding to the ribosome; instead it prevents physiological conformation of the 48S PIC by restricting the ribosome head domain rotation.

Our results explain how Nsp1 inhibits protein synthesis; however, how SARS-CoV-2 escapes this inhibition and initiate translation of its own RNA remains unanswered. The 5′ UTR of SARS-CoV is essential for escaping Nsp1-mediated suppression of translation (Tanaka et al., 2012). Interactions involving the viral 5′ UTR presumably result in the "unplugging" of Nsp1 from the 40S ribosome during the initiation of viral translation. In addition, the weakening of eIF3 binding to the 40S subunit is beneficial for translation initiation of some viruses. The hepatitis C virus (HCV) IRES displaces eIF3 from the interface of the 40S subunit to load its RNA in the mRNA-binding channel (Hashem et al., 2013; Niepmann and Gerresheim, 2020). HCV IRES interacts with eIF3a, eIF3c, and other core subunits of eIF3 to promote formation of the viral 48S PIC (Cate, 2017). The eIF3d subunit of the eIF3 complex can be cross-linked to the mRNA in the exit channel of the 48S PIC, and it has its own cap-binding activity, which can replace the canonical eIF4E-dependent pathway and promote translation of selected cellular mRNAs (Lee et al., 2016; Pisarev et al., 2008; Walker et al., 2020). Interestingly, a recent genome-wide CRISPR screen revealed the eIF3a and eIF3d are essential for SARS-CoV-2 infection (Wei et al., 2020). The requirement of the same essential initiation factors suggests that it is possible that SARS-CoV-2 may use an "IRES-like" mechanism involving eIF3 recruitment by 5′ UTR to overcome Nsp1 inhibition. Binding of 5′ UTR may cause conformational change of the 40S head leading to the latch opening, Nsp1 dissociation, viral RNA loading into mRNA-binding channel, and formation of the functional 80S initiation complex primed for viral protein synthesis. However, the detailed mechanisms of viral escape of Nsp1 inhibition must await future experimental studies.

Limitations of Study

The transcriptome changes were observed in the presence of Nsp1 in the cells of human lung origin. However, the role of the transcriptome changes in the loss of cell viability is still not understood. To elucidate the mechanism of translation inhibition by Nsp1, we determined the cryo-EM structure of rabbit 40S ribosomal subunit complex with Nsp1. The atomic structure of C-Nsp1 was built into well-defined high-resolution density, while only global density of the N-Nsp1 was observed. Further work is needed to reveal the details and the potential functional consequence of the interaction of N-Nsp1 and 40S ribosome subunit. Our results suggested potential mechanisms of SARS-CoV-2 translation initiation, but future experiments are needed to illustrate how SARS-CoV-2 overcomes the Nsp1 inhibition and starts the translation of its own genome.

STAR★METHODS

Detailed methods are provided in the online version of this paper and include the following:

- KEY RESOURCES TABLE
- RESOURCE AVAILABILITY
  - Lead Contact
  - Material Availability
  - Data and Code Availability
- EXPERIMENTAL MODEL AND SUBJECT DETAILS
  - Mammalian cells
  - E. coli
- METHOD DETAILS
  - SARS-CoV-2 plasmid cloning
  - Nsp1 mutant ORF construction
  - Generation of stable cell lines
  - Mammalian cell culture
  - SARS-CoV-2 ORF mini-screen for cell viability
  - Determination of luciferase reporter cell viability
  - Electroporation with 4D nucleofection
  - Apoptosis flow cytometry assay
  - Gene expression analysis by mRNA sequencing (mRNA-seq, RNA-seq)
  - mRNA-seq data processing, differential expression analysis and pathway analysis
  - RT-qPCR
  - Ribosome and CrPV IRES purification
  - Protein construction, expression and purification
  - Filter binding assays
  - Cryo-EM sample preparation, data collection and processing
  - Model building and refinement
- QUANTIFICATION AND STATISTICAL ANALYSIS
  - Sample size determination
  - Replication
  - Standard statistical analysis

SUPPLEMENTAL INFORMATION

Supplemental Information can be found online at https://doi.org/10.1016/j.molcel.2020.10.034.

ACKNOWLEDGMENTS

We thank the Yale cryo-EM facilities for assistance with data collection. We thank the Xiong lab and Chen lab members for discussions. We thank Drs. Krogan and Gordon for generously providing the initial cDNA templates of SARS-CoV-2 ORFs. We thank Xiaoyun Dai, Lupeng Ye, Paul Clark, and several others for sharing various plasmids and reagents. We thank the Yale Center for Genome Analysis and Center for Research Computing for providing high-throughput sequencing and computing assistance and resources. This work was supported by Yale University discretionary funds to Y.X. and S.C. The lab of S.C. is also supported by the NIH (DP2CA238295, 1R01CA231112, U54CA209992-8697, R33CA225498, and RF1DA048811) and the U.S. Department of Defense (DoD) (W81XWH2010072 and PR201784).

AUTHOR CONTRIBUTIONS

S.Y., L.P., S.C., I.B.L., and Y.X. initiated the project and designed the experiments. S.Y., I.B.L., Q.S., and Y.H. produced proteins and 40S ribosomal subunit. S.Y. and S.C.D. performed binding assays. S.Y. prepared the cryo-EM samples. Y.H. and S.W. carried out cryo-EM data collection. S.Y. and Y.X. did cryo-EM data processing. S.Y., I.B.L., S.C.D., and Y.X. analyzed cryo-EM structure. L.P. and M.B.D. performed cellar assays. L.P. and J.J.P. performed and processed mRNA-seq. S.Y., L.P., S.C., I.B.L., and Y.X. prepared the manuscript. S.C., I.B.L., and Y.X. jointly supervised the work.

DECLARATION OF INTERESTS

The authors declare no competing interests.

Received: August 11, 2020
Revised: October 5, 2020
Accepted: October 22, 2020
Published: October 29, 2020

REFERENCES

Adams, P.D., Afonine, P.V., Bunkóczi, G., Chen, V.B., Davis, I.W., Echols, N., Headd, J.J., Hung, L.W., Kapral, G.J., Grosse-Kunstleve, R.W., et al. (2010). PHENIX: a comprehensive Python-based system for macromolecular structure solution. Acta Crystallogr. D Biol. Crystallogr. *66*, 213–221.

Almeida, M.S., Johnson, M.A., Herrmann, T., Geralt, M., and Wüthrich, K. (2007). Novel beta-barrel fold in the nuclear magnetic resonance structure of the replicase nonstructural protein 1 from the severe acute respiratory syndrome coronavirus. J. Virol. *81*, 3151–3161.

Astuti, I., and Ysrafil. (2020). Severe acute respiratory syndrome coronavirus 2 (SARS-CoV-2): an overview of viral structure and host response. Diabetes Metab. Syndr. *14*, 407–412.

Aylett, C.H., Boehringer, D., Erzberger, J.P., Schaefer, T., and Ban, N. (2015). Structure of a yeast 40S-eIF1-eIF1A-eIF3-eIF3j initiation complex. Nat. Struct. Mol. Biol. *22*, 269–271.

Babaylova, E., Malygin, A., Gopanenko, A., Graifer, D., and Karpova, G. (2019). Tetrapeptide 60-63 of human ribosomal protein uS3 is crucial for translation initiation. Biochim. Biophys. Acta Gene Regul. Mech. *1862*, 194411.

Blanco-Melo, D., Nilsson-Payant, B.E., Liu, W.C., Uhl, S., Hoagland, D., Moller, R., Jordan, T.X., Oishi, K., Panis, M., Sachs, D., et al. (2020). Imbalanced host response to SARS-CoV-2 drives development of COVID-19. Cell *181*, 1036–1045.e9.

Bray, N.L., Pimentel, H., Melsted, P., and Pachter, L. (2016). Near-optimal probabilistic RNA-seq quantification. Nat. Biotechnol. *34*, 525–527.

Cate, J.H. (2017). Human eIF3: from 'blobology' to biological insight. Philos. Trans. R. Soc. Lond. B Biol. Sci. *372*, 20160176.

Chandrasekaran, V., Juszkiewicz, S., Choi, J., Puglisi, J.D., Brown, A., Shao, S., Ramakrishnan, V., and Hegde, R.S. (2019). Mechanism of ribosome stalling during translation of a poly(A) tail. Nat. Struct. Mol. Biol. *26*, 1132–1140.

Coronaviridae Study Group of the International Committee on Taxonomy of Viruses (2020). The species severe acute respiratory syndrome-related coronavirus: classifying 2019-nCoV and naming it SARS-CoV-2. Nat. Microbiol. *5*, 536–544.

Dong, J., Aitken, C.E., Thakur, A., Shin, B.S., Lorsch, J.R., and Hinnebusch, A.G. (2017). Rps3/uS3 promotes mRNA binding at the 40S ribosome entry channel and stabilizes preinitiation complexes at start codons. Proc. Natl. Acad. Sci. U S A *114*, E2126–E2135.

Emsley, P., Lohkamp, B., Scott, W.G., and Cowtan, K. (2010). Features and development of Coot. Acta Crystallogr. D Biol. Crystallogr. *66*, 486–501.

Fraser, C.S., Lee, J.Y., Mayeur, G.L., Bushell, M., Doudna, J.A., and Hershey, J.W.B. (2004). The j-subunit of human translation initiation factor eIF3 is required for the stable binding of eIF3 and its subcomplexes to 40 S ribosomal subunits in vitro. J. Biol. Chem. *279*, 8946–8956.

Fraser, C.S., Berry, K.E., Hershey, J.W.B., and Doudna, J.A. (2007). eIF3j is located in the decoding center of the human 40S ribosomal subunit. Mol. Cell *26*, 811–819.

Gordon, D.E., Jang, G.M., Bouhaddou, M., Xu, J., Obernier, K., White, K.M., O'Meara, M.J., Rezelj, V.V., Guo, J.Z., Swaney, D.L., et al. (2020). A SARS-CoV-2 protein interaction map reveals targets for drug repurposing. Nature *583*, 459–468.

Graifer, D., Malygin, A., Zharkov, D.O., and Karpova, G. (2014). Eukaryotic ribosomal protein S3: A constituent of translational machinery and an extraribosomal player in various cellular processes. Biochimie *99*, 8–18.

Haimov, O., Sinvani, H., Martin, F., Ulitsky, I., Emmanuel, R., Tamarkin-Ben-Harush, A., Vardy, A., and Dikstein, R. (2017). Efficient and accurate translation initiation directed by TISU involves RPS3 and RPS10e binding and differential eukaryotic initiation factor 1A regulation. Mol. Cell. Biol. *37*, e00150-17.

Hashem, Y., des Georges, A., Dhote, V., Langlois, R., Liao, H.Y., Grassucci, R.A., Pestova, T.V., Hellen, C.U., and Frank, J. (2013). Hepatitis-C-virus-like internal ribosome entry sites displace eIF3 to gain access to the 40S subunit. Nature *503*, 539–543.

Hershey, J.W. (2015). The role of eIF3 and its individual subunits in cancer. Biochim. Biophys. Acta *1849*, 792–800.

Hertz, M.I., and Thompson, S.R. (2011). Mechanism of translation initiation by Dicistroviridae IGR IRESs. Virology *411*, 355–361.

Hinnebusch, A.G. (2014). The scanning mechanism of eukaryotic translation initiation. Annu. Rev. Biochem. *83*, 779–812.

Hinnebusch, A.G. (2017). Structural insights into the mechanism of scanning and start codon recognition in eukaryotic translation initiation. Trends Biochem. Sci. *42*, 589–611.

Hinnebusch, A.G., Ivanov, I.P., and Sonenberg, N. (2016). Translational control by 5′-untranslated regions of eukaryotic mRNAs. Science *352*, 1413–1416.

Hoffmann, M., Kleine-Weber, H., Schroeder, S., Krüger, N., Herrler, T., Erichsen, S., Schiergens, T.S., Herrler, G., Wu, N.H., Nitsche, A., et al. (2020). SARS-CoV-2 cell entry depends on ACE2 and TMPRSS2 and is blocked by a clinically proven protease inhibitor. Cell *181*, 271–280.e8.

Huang, D.W., Sherman, B.T., and Lempicki, R.A. (2009). Systematic and integrative analysis of large gene lists using DAVID bioinformatics resources. Nature Protocols *4*, 44–57.

Huang, D.W., Sherman, B.T., Tan, Q., Collins, J.R., Alvord, W.G., Roayaei, J., Stephens, R., Baseler, M.W., Lane, H.C., and Lempicki, R.A. (2007). The DAVID Gene Functional Classification Tool: a novel biological module-centric algorithm to functionally analyze large gene lists. Genome Biol. *8*, R183.

Huang, C., Lokugamage, K.G., Rozovics, J.M., Narayanan, K., Semler, B.L., and Makino, S. (2011). SARS coronavirus nsp1 protein induces template-dependent endonucleolytic cleavage of mRNAs: viral mRNAs are resistant to nsp1-induced RNA cleavage. PLoS Pathog. *7*, e1002433.

Jan, E., Mohr, I., and Walsh, D. (2016). A cap-to-tail guide to mRNA translation strategies in virus-infected cells. Annu. Rev. Virol. *3*, 283–307.

Kamitani, W., Narayanan, K., Huang, C., Lokugamage, K., Ikegami, T., Ito, N., Kubo, H., and Makino, S. (2006). Severe acute respiratory syndrome coronavirus nsp1 protein suppresses host gene expression by promoting host mRNA degradation. Proc. Natl. Acad. Sci. U S A *103*, 12885–12890.

Kamitani, W., Huang, C., Narayanan, K., Lokugamage, K.G., and Makino, S. (2009). A two-pronged strategy to suppress host protein synthesis by SARS coronavirus Nsp1 protein. Nat. Struct. Mol. Biol. *16*, 1134–1140.

Kim, D., Lee, J.Y., Yang, J.S., Kim, J.W., Kim, V.N., and Chang, H. (2020). The architecture of SARS-CoV-2 transcriptome. Cell *181*, 914–921.e10.

Lee, A.S., Kranzusch, P.J., Doudna, J.A., and Cate, J.H. (2016). eIF3d is an mRNA cap-binding protein that is required for specialized translation initiation. Nature *536*, 96–99.

Lim, Y.X., Ng, Y.L., Tam, J.P., and Liu, D.X. (2016). Human coronaviruses: a review of virus-host interactions. Diseases *4*, 26.

Lokugamage, K.G., Narayanan, K., Huang, C., and Makino, S. (2012). Severe acute respiratory syndrome coronavirus protein nsp1 is a novel eukaryotic translation inhibitor that represses multiple steps of translation initiation. J. Virol. *86*, 13598–13608.

Lomakin, I.B., and Steitz, T.A. (2013). The initiation of mammalian protein synthesis and mRNA scanning mechanism. Nature *500*, 307–311.

Lozano, G., and Martínez-Salas, E. (2015). Structural insights into viral IRES-dependent translation mechanisms. Curr. Opin. Virol. *12*, 113–120.

Martinez-Salas, E., Francisco-Velilla, R., Fernandez-Chamorro, J., and Embarek, A.M. (2018). Insights into structural and mechanistic features of viral IRES elements. Front. Microbiol. *8*, 2629.

Masters, P.S. (2006). The molecular biology of coronaviruses. Adv. Virus Res. *66*, 193–292.

Mastronarde, D.N. (2005). Automated electron microscope tomography using robust prediction of specimen movements. J. Struct. Biol. *152*, 36–51.

Murray, J., Savva, C.G., Shin, B.S., Dever, T.E., Ramakrishnan, V., and Fernández, I.S. (2016). Structural characterization of ribosome recruitment and translocation by type IV IRES. eLife *5*, e13567.

Narayanan, K., Huang, C., Lokugamage, K., Kamitani, W., Ikegami, T., Tseng, C.T., and Makino, S. (2008). Severe acute respiratory syndrome coronavirus nsp1 suppresses host gene expression, including that of type I interferon, in infected cells. J. Virol. *82*, 4471–4479.

Niepmann, M., and Gerresheim, G.K. (2020). Hepatitis C virus translation regulation. Int. J. Mol. Sci. *21*, 21.

Passmore, L.A., Schmeing, T.M., Maag, D., Applefield, D.J., Acker, M.G., Algire, M.A., Lorsch, J.R., and Ramakrishnan, V. (2007). The eukaryotic translation initiation factors eIF1 and eIF1A induce an open conformation of the 40S ribosome. Mol. Cell *26*, 41–50.

Pettersen, E.F., Goddard, T.D., Huang, C.C., Couch, G.S., Greenblatt, D.M., Meng, E.C., and Ferrin, T.E. (2004). UCSF Chimera—a visualization system for exploratory research and analysis. J. Comput. Chem. *25*, 1605–1612.

Pimentel, H., Bray, N.L., Puente, S., Melsted, P., and Pachter, L. (2017). Differential analysis of RNA-seq incorporating quantification uncertainty. Nat. Methods *14*, 687–690.

Pisarev, A.V., Kolupaeva, V.G., Yusupov, M.M., Hellen, C.U., and Pestova, T.V. (2008). Ribosomal position and contacts of mRNA in eukaryotic translation initiation complexes. EMBO J. *27*, 1609–1621.

Punjani, A., Rubinstein, J.L., Fleet, D.J., and Brubaker, M.A. (2017). cryoSPARC: algorithms for rapid unsupervised cryo-EM structure determination. Nat. Methods *14*, 290–296.

Schrödinger, LLC (2015). The PyMOL Molecular Graphics System, version 1.8. https://pymol.org/2/.

Schubert, K., Karousis, E.D., Jomaa, A., Scaiola, A., Echeverria, B., Gurzeler, L.A., Leibundgut, M., Thiel, V., Muhlemann, O., and Ban, N. (2020). SARS-CoV-2 Nsp1 binds the ribosomal mRNA channel to inhibit translation. Nat. Struct. Mol. Biol. *27*, 959–966.

Sharifulin, D.E., Grosheva, A.S., Bartuli, Y.S., Malygin, A.A., Meschaninova, M.I., Ven'yaminova, A.G., Stahl, J., Graifer, D.M., and Karpova, G.G. (2015). Molecular contacts of ribose-phosphate backbone of mRNA with human ribosome. Biochim. Biophys. Acta *1849*, 930–939.

Sharifulin, D.E., Bartuli, Y.S., Meschaninova, M.I., Ven'yaminova, A.G., Graifer, D.M., and Karpova, G.G. (2016). Exploring accessibility of structural elements of the mammalian 40S ribosomal mRNA entry channel at various steps of translation initiation. Biochim. Biophys. Acta *1864*, 1328–1338.

Sievers, F., Wilm, A., Dineen, D., Gibson, T.J., Karplus, K., Li, W., Lopez, R., McWilliam, H., Remmert, M., Söding, J., et al. (2011). Fast, scalable generation of high-quality protein multiple sequence alignments using Clustal Omega. Molecular Systems Biology *7*, 539.

Sokabe, M., and Fraser, C.S. (2014). Human eukaryotic initiation factor 2 (eIF2)-GTP-Met-tRNAi ternary complex and eIF3 stabilize the 43 S preinitiation complex. J. Biol. Chem. *289*, 31827–31836.

Subramanian, A., Tamayo, P., Mootha, V.K., Mukherjee, S., Ebert, B.L., Gillette, M.A., Paulovich, A., Pomeroy, S.L., Golub, T.R., Lander, E.S., and Mesirov, J.P. (2005). Gene set enrichment analysis: a knowledge-based approach for interpreting genome-wide expression profiles. Proc. Natl. Acad. Sci. U S A *102*, 15545–15550.

Tanaka, T., Kamitani, W., DeDiego, M.L., Enjuanes, L., and Matsuura, Y. (2012). Severe acute respiratory syndrome coronavirus nsp1 facilitates efficient propagation in cells through a specific translational shutoff of host mRNA. J. Virol. *86*, 11128–11137.

Thoms, M., Buschauer, R., Ameismeier, M., Koepke, L., Denk, T., Hirschenberger, M., Kratzat, H., Hayn, M., Mackens-Kiani, T., Cheng, J., et al. (2020a). Structural basis for translational shutdown and immune evasion by the Nsp1 protein of SARS-CoV-2. Science *369*, 1249–1255.

Tohya, Y., Narayanan, K., Kamitani, W., Huang, C., Lokugamage, K., and Makino, S. (2009). Suppression of host gene expression by nsp1 proteins of group 2 bat coronaviruses. J. Virol. *83*, 5282–5288.

Walker, M.J., Shortridge, M.D., Albin, D.D., Cominsky, L.Y., and Varani, G. (2020). Structure of the RNA specialized translation initiation element that recruits eIF3 to the 5′-UTR of c-Jun. J. Mol. Biol. *432*, 1841–1855.

Walsh, D., and Mohr, I. (2011). Viral subversion of the host protein synthesis machinery. Nat. Rev. Microbiol. *9*, 860–875.

Wathelet, M.G., Orr, M., Frieman, M.B., and Baric, R.S. (2007). Severe acute respiratory syndrome coronavirus evades antiviral signaling: role of nsp1 and rational design of an attenuated strain. J. Virol. *81*, 11620–11633.

Wei, J., Alfajaro, M.M., Hanna, R.E., DeWeirdt, P.C., Strine, M.S., Lu-Culligan, W.J., Zhang, S.-M., Graziano, V.R., Schmitz, C.O., Chen, J.S., et al. (2020). Genome-wide CRISPR screen reveals host genes that regulate SARS-CoV-2 infection. bioRxiv. https://doi.org/10.1101/2020.2006.2016.155101.

Wong, H.H., Kumar, P., Tay, F.P.L., Moreau, D., Liu, D.X., and Bard, F. (2015). Genome-wide screen reveals valosin-containing protein requirement for coronavirus exit from endosomes. J. Virol. *89*, 11116–11128.

Yoshimoto, F.K. (2020). The proteins of severe acute respiratory syndrome coronavirus-2 (SARS CoV-2 or n-COV19), the cause of COVID-19. Protein J. *39*, 198–216.

Zhou, P., Yang, X.L., Wang, X.G., Hu, B., Zhang, L., Zhang, W., Si, H.R., Zhu, Y., Li, B., Huang, C.L., et al. (2020). A pneumonia outbreak associated with a new coronavirus of probable bat origin. Nature *579*, 270–273.

Ziebuhr, J. (2005). The coronavirus replicase. Curr. Top. Microbiol. Immunol. *287*, 57–94.

Züst, R., Cervantes-Barragán, L., Kuri, T., Blakqori, G., Weber, F., Ludewig, B., and Thiel, V. (2007). Coronavirus non-structural protein 1 is a major pathogenicity factor: implications for the rational design of coronavirus vaccines. PLoS Pathog. *3*, e109.

STAR★METHODS

KEY RESOURCES TABLE

REAGENT or RESOURCE	SOURCE	IDENTIFIER
Antibodies		
Cleaved Caspase-3 (Asp175) Antibody	Cell Signaling	Cat#9669s; RRID:AB_2341188
Bacterial and Virus Strains		
E. coli BL21(DE3)	Lucigen	Cat#60401
E. coli XL10-Gold Ultracompetent Cells	Agilent	Cat#200315
One shot Stbl3 Chemical Competent cells E.coli	ThermoFisher	Cat#C737303
Chemicals, Peptides, and Recombinant Proteins		
Terrific Broth	Research Products International	Cat#T5100-5000.0
Luria Broth	Research Products International	Cat#L24400
Isopropyl β-D-1-thiogalactopyranoside (IPTG)	American Bioanalytical	Cat#AB00841-00010
NuPAGE LDS Sample Buffer (4X)	Thermo Fisher	Cat#NP0008
Dithiothreitol (DTT)	American Bioanalytical	Cat#AB00490-00100
SimplyBlue SafeStain	Thermo Fisher	Cat#LC6060
KOD Hot Start DNA polymerase	Novagen	Cat#710863
Rabbit 40S ribosome	Lomakin and Steitz, 2013	N/A
Recombinant Nsp1	This paper	N/A
Recombinant eIF3j	This paper	N/A
DPBS, no calcium, no magnesium	GIBCO	Cat#14190250
DMEM, high glucose,pyruvate	GiBCO	Cat#11995065
Fetal Bovine Serum	Corning	Cat#35-011-CV
Penicillin-Streptomycin (10,000 U/mL)	GIBCO	Cat#15140122
QIAquick gel extraction KIt	QIAGEN	Cat#28706
E-Gel Low Range Quantitative DNA Ladder	ThermoFisher	Cat#12373031
Gibson Assembly Master Mix	NEB	Cat#E2611
Phusion Flash High-Fidelity PCR Master Mix	ThermoFisher	Cat#F548L
QIAGEN Plasmid Maxi Kit	QIAGEN	Cat#12162
Fixation/Permeabilization Solution Kit	BD	Cat#554714
FastDigest BshTI	ThermoFisher	Cat#FD1464
FastDigest BstXI	ThermoFisher	Cat#FD1024
FastDigest XhoI	ThermoFisher	Cat#FD0694
FastDigest KpnI	ThermoFisher	Cat#FD0524
CellTiter-Glo® Luminescent Cell Viability Assay	Promega	Cat#G7572
SF Cell Line 4D-NucleofectorTM X Kit L	Lonza	Cat# V4XC-2012
RNeasy Plus Mini Kit (250)	QIAGEN	Cat# 74136
NEBNext Ultra II Directional RNA Library Prep Kit for Illumina	NEB	Cat# E7760S
NEBNext® Multiplex Oligos for Illumina® (Index Primers Set 1)	NEB	Cat# E7335S
XenoLight D-Luciferin - K+ Salt Bioluminescent Substrate	Perkin Elmer	Cat#122799
M-MLV Reverse Transcriptase	Sigma	Cat# 11062603001
Deposited Data		
Structure of the Nsp1-40S complex	This paper	PDB: 7JQB
Structure of the Nsp1-40S-CrPV IRES complex	This paper	PDB: 7JQC
Cryo-EM map of the Nsp1-40S complex	This paper	EMD: 22432

(*Continued on next page*)

Continued

REAGENT or RESOURCE	SOURCE	IDENTIFIER
Cryo-EM map of the Nsp1-40S-CrPV IRES complex	This paper	EMD: 22433
Source data and summary statistics of cellular viability effect by introduction of SARS-CoV-2 viral proteins and mutants	This paper	Table S2
Processed Nsp1 mRNA-seq dataset and differential expression analysis	This paper	Table S3 GEO/SRA accession number: PRJNA667046
DAVID pathway analysis of Nsp1 differentially expressed gene sets	This paper	Table S4
Experimental Models: Cell Lines		
H1299	ATCC	ATCC® CRL-5803
VeroE6	ATCC	ATCC® CRL-1586
Oligonucleotides		
All standard cloning primers for Gibson assembly	This paper	Table S1
Amplicon primers for cloning	This paper	Table S1
ACTB (hs01060665_g1)	Thermo Fisher	Cat#4331182
NSP1 Taqman Probe	Invitrogen	In this paper
Recombinant DNA		
pETDUET-1	EMD Millipore	Cat#71146
pMAL system	New England Biolabs	Cat#E8200S
Plasmid: 6xHis-Nsp1 in pETDUET-1	This paper	N/A
Plasmid: 6xHis-MBP-Nsp1 in pMAT9S (lab-made p-MAL derivative)	This paper	N/A
Plasmid: 6xHis-eIF3j in pETDUET-1	This paper	N/A
pcDNA3.1	Addgene	Cat#52535
pVPSB empty	This paper	N/A
pVPSB-ORFs	This paper	N/A
Nsp1 mutant1	This paper	N/A
Nsp1 mutant3	This paper	N/A
Nsp1 mutant4	This paper	N/A
Lenti-Fluc-Puro	This paper	N/A
Software and Algorithms		
Phenix (v1.18.2)	Adams et al., 2010	https://www.phenix-online.org/
Coot	Emsley et al., 2010	https://www2.mrc-lmb.cam.ac.uk/personal/pemsley/coot/
cryoSPARC (v2.15)	Punjani et al., 2017	https://cryosparc.com/
PyMOL (v2.1)	Schrödinger, LLC, 2015	https://pymol.org/2/
Chimera (v1.14)	Pettersen et al., 2004	https://www.cgl.ucsf.edu/chimera/
SerialEM	Mastronarde, 2005	https://bio3d.colorado.edu/SerialEM/
NanoAnalyze (v3.6.0)	TA Instruments	https://www.tainstruments.com/support/software-downloads-support/downloads/
Clustal Omega	Sievers et al., 2011	https://www.ebi.ac.uk/Tools/msa/clustalo/
FlowJo software 9.9.6	FlowJo	https://www.flowjo.com
Kallisto 0.45.0	Bray et al., 2016	https://pachterlab.github.io/kallisto/
Sleuth 0.30.0	Pimentel et al., 2017	https://pachterlab.github.io/sleuth/about
DAVID 6.8	Huang et al., 2009	https://david.ncifcrf.gov/
GSEA 4.0.3	Subramanian et al., 2005	https://www.gsea-msigdb.org/gsea/index.jsp

(*Continued on next page*)

Continued

REAGENT or RESOURCE	SOURCE	IDENTIFIER
Other		
Ni-NTA Agarose	QIAGEN	Cat#30230
HiTrap Q HP 5mL	GE Healthcare	Cat#17115401
HiLoad 16/600 Superdex 75 PG	GE Healthcare	Cat#28989333
NuPAGE 4-12% Bis-Tris Midi gels	Invitrogen	Cat#WG1403B0X
Protein Concentrators PES, 100K MWCO	Thermo Scientific	Cat#88503
Amicon Ultra-15 Centrifugal Filter Units 10kDa	Millipore Sigma	Cat#UFC901024
C-flat Holey Carbon for Cryo-TEM	Electron Microscopy Sciences	Cat#312-50

RESOURCE AVAILABILITY

Lead Contact

Further information and requests for resources and reagents should be directed to and will be fulfilled by the Lead Contact, Yong Xiong (yong.xiong@yale.edu).

Material Availability

All unique/stable reagents generated in this study are available from the Lead Contact.

Data and Code Availability

All data generated or analyzed during this study are included in this article and its supplementary information files. Specifically, source data and statistics for non-high-throughput experiments are provided in a supplementary table excel file (Table S2). High-throughput experiment data are provided as processed quantifications in Supplemental Datasets (Tables S3 and S4). Genomic sequencing raw data are deposited to NIH Sequence Read Archive (SRA) and/or Gene Expression Omnibus (GEO) and the accession code is PRJNA667046. Constructs are available at either through a public repository or via requests to the corresponding authors. Original cell lines are available at commercial sources listed in supplementary information files. Genetically modified cell lines are available via the authors' laboratories. Codes that support the findings of this research are being deposited to a public repository such as GitHub, and are available from the corresponding authors upon reasonable request.

The cryo-EM maps of the Nsp1-40S ribosome complex and the Nsp1-40S-CrPV IRES ribosome complex have been deposited in the Electron Microscopy Data Bank as EMD-22432 and EMD-22433, respectively. The corresponding structure models are in the Protein Data Bank with accession code PDB: 7JQB, PDB: 7JQC. Additional Supplemental Items are available from Mendeley Data at https://doi.org/10.17632/642gjvx74d.1.

EXPERIMENTAL MODEL AND SUBJECT DETAILS

Mammalian cells

H1299, H1299-PL, Vero E6, Vero E6-PL cell lines were used in the cell viability assay and the mRNA sequencing.

E. coli

E. coli BL21(DE3) was used for the expression of recombinant Nsp1 and eIF3j.

METHOD DETAILS

SARS-CoV-2 plasmid cloning

The initial cDNA templates of SARS-CoV-2 ORF gene containing plasmids were provided by Dr. Krogan as a gift (Gordon et al., 2020), where the ORFs were primarily cloned into lentiviral expression vector. A non-viral expression vector, pVPSB empty, where ORFs were driven by a constitutive EFS promoter and terminated by a short poly A, was constructed by cloning gBlock fragments (IDT) into pcDNA3.1 vector (Addgene, #52535) by the Gibson assembly (NEB). All ORFs gene encoding fragments were PCR amplified from the lentiviral vectors with ORF-specific forward primers and common reverse primer that containing overlaps that corresponded to flanking sequences of the and KpnI and XhoI restriction sites in the pVPSB empty vector. The primer lists were provided in Table S1. ORFs PCR amplified fragments were gel-purified and cloned into restriction enzyme digested backbone by the Gibson assembly (NEB). A lentiviral vector constitutively expressing a Firefly Luciferase and a puromycin mammalian selection marker (Lenti-Fluc-Puro) was generated by standard molecular cloning. All plasmids were sequenced and harvested by Maxiprep for following assay.

Nsp1 mutant ORF construction

Truncation mutant Nsp1 has triple stop codons introduced after residues 12 (N-terminal mutant). Nsp1 mutant3 has R124 and K125 replaced with S124 and E125 (R124S/K125E). Nsp1 mutant4 has N128 and K129 were converted to S128 and E129 (N128S/K129E). IDT gBlocks were ordered for truncated Nsp1 and different Nsp1 mutants with 19∼23 bp overlaps that corresponded to flanking sequences of the and AgeI and BstXI restriction sites in the pVPSBA01-Nsp1 plasmid. pVPSBA01-Nsp1 plasmid were digested and gel purified, and gBlocks were cloned using the Gibson assembly (NEB).

Generation of stable cell lines

Lentivirus was produced by transfection of co-transgene plasmid (Lenti-Fluc-Puro) and packaging plasmids (psPAX2, pMD2.G) into HEK293FT cells, followed by supernatant harvesting, filtering and concentration with Amicon filters (Sigma). H1299 and Vero E6 cells were infected with Lenti-Fluc-Puro lentivirus. After 24 h of virus transduction, cells were selected with 10 μg/mL puromycin, until all cells died in the control group. Luc expressing H1299 and Vero E6 that with puromycin resistance cell lines were obtained and named as H1299-PL and Vero E6-PL (Vero E6-PL for short) respectively.

Mammalian cell culture

H1299, H1299-PL, Vero E6, Vero E6-PL cell lines were cultured in Dulbecco's modified Eagle's medium (DMEM; Thermo fisher) supplemented with 10% Fetal bovine serum (FBS, Hyclone),1% penicillin-streptomycin (GIBCO), named as D10 medium. Cells were typically passaged every 1-2 days at a split ratio of 1:2 or 1:4 when the confluency reached at 80%.

SARS-CoV-2 ORF mini-screen for cell viability

H1299 cells were plated in white opaque walled microwell assay plates, 25,000 cells per 96 well. SARS-CoV-2 ORF plasmids, 1 μg of each, were parallelly transfected with 1 μL lipofectamine 2000, in triplicates. Cell viability was detected at every 24hr after transfection using CellTiter-Glo® Luminescent Cell Viability Assay kit (Promega). Relative viability was normalized to the mean viability of empty vector transfected control group. All procedures followed the manufacturer standard protocol. Luminescent signals were measured by a Plate Reader (PerkinElmer).

Determination of luciferase reporter cell viability

H1299-PL and Vero E6-PL cells were plated in white opaque walled microwell assay plates, 25,000 cells per well in a 96 well. SARS-CoV-2 ORF plasmids, 1 μg of each, were parallelly transfected with 1ul lipofectamine 2000. Cell viability was measured every 24 hr after plasmid transfection by adding 150 μg / ml D-Luciferin (PerkinElmer) using a multi-channel pipette. Luciferase intensity was measured by a Plate Reader (PerkinElmer).

Electroporation with 4D nucleofection

Cells were trypsinized and collected, 1e6 cells were resuspended in SF cell line NucleofectorTM solution with 3 μg plasmid DNA. Cells were transferred into 100 μl NucleocuvetteTM Vessel and NCI-H1299 [H1299] cell specific protocol were utilized according to the manufacturer's protocol (4D-NucleofectorTM X Unit, Lonza). After the pulse application, 100 μL prewarmed D10 medium was added to the electroporated cells in the cuvette. Cells were gently resuspended in the cuvette and transferred into 6 well plate, cultured in incubator. Cells were collected at 24 or 48 hours later for flowcytometry assay and RNA extraction.

Apoptosis flow cytometry assay

Flow cytometry was performed using standard immunology protocols. Briefly, experimental and control cells were electroporated with respective plasmids. After a defined time point, cells were collected, fixed and permeabilized using Fixation/Permeablization Solution kit (BD). Then antigen-specific antibodies with specific dilutions were added into cells and incubated for 30 min on ice. Cells were washed with cold MACS buffer for 3 times before analyzed on a BD FACSAria cytometer. Antibody used: anti-cleaved Caspase-3(Asp175) (Sigma, 9669s, 1:200).

Gene expression analysis by mRNA sequencing (mRNA-seq, RNA-seq)

For H1299-PL cells electroporated with Nsp1 or Nsp1 mutant, mRNA-seq libraries were prepared following next-generation sequencing (NGS) protocols. Briefly, 1e6 H1299 cells were electroporated with 3 μg Nsp1, mutant Nsp1, and relative control plasmids. Electroporation was done in with quadruplicates for each group. Cells were collected 24hr post electroporation. Total mRNA was extracted with RNasy Plus Mini Kit (QIAGEN). 1 μg total mRNA each sample was used for the RNA-seq library preparations. A NEBNext® Ultra RNA Library Prep Kit for Illumina was employed to perform RNA-seq library preparation and samples were multiplexed using barcoded primers provided by NEBNext® Multiplex Oligos for Illumina® (Index Primers Set 1). All procedures follow the manufacturer standard protocol. Libraries were sequenced with Novaseq system (Illumina).

mRNA-seq data processing, differential expression analysis and pathway analysis

The mRNA data processing, transcript quantification, differential expression, and pathway analysis were performed using custom computational programs. In brief, Fastq files from mRNA-seq were used analyzed using the Kallisto quant algorithm for transcript

quantification (Bray et al., 2016). Differential expression analysis was performed using Sleuth (Pimentel et al., 2017). Z-scores for time course heatmap were calculated by log2-normalizion of gene counts following by scaling by genes. Visualizations of differentially expressed genes such as volcano plots and heatmaps were generated using standard R packages. Differentially upregulated and downregulated genes were subjected to pathway analysis by DAVID (Huang et al., 2007) and/or GSEA (Subramanian et al., 2005). Processed mRNA-seq data, differential expression analysis and pathway analysis results are provided in (Tables S3 and S4).

RT-qPCR

Total RNA was extracted from cells using RNasy Plus Mini Kit (QIAGEN). Total mRNA was reverse transcribed into cDNA by M-MLV Reverse Transcriptase (Sigma). Samples were collected in triplicates. Gene expression was quantified using Taqman Fast Universal PCR Master Mix (Thermo Fisher) and Taqman probes (Invitrogen). NSP1 probe was generated with custom designed according to the Nsp1 DNA sequence in the SARS-CoV-2 genome annotation (2019-nCoV/USA-WA1/2020, accession MN985325). RNA expression level was normalized to *ACTB* (human). Relative mRNA expression was determined via the $\Delta\Delta C_t$ method.

Ribosome and CrPV IRES purification

40S ribosomal subunits were purified from the rabbit reticulocyte lysate (Green Hectares, USA) as described previously (Lomakin and Steitz, 2013). The gene for wild-type CrPV IRES (nucleotides 6028-6240) was chemically synthesized and cloned in the pBluescript SK vector flanked at the 5′ end by a T7 promoter sequence and an EcoRI cleavage site at the 3′ end. Standard *in vitro* transcription protocol was used for IRES RNA synthesis and purification (MEGAscript T7 Transcription Kit, Ambion, USA).

Protein construction, expression and purification

Full-length SARS-CoV-2 Nsp1 was cloned into pMAT-9 s vector and pET-Duet vector for expression of MBP-tagged and 6 × his tagged proteins, respectively. The *Escherichia coli* BL21 (DE3) cells were used for protein expressions, which were induced by 0.5 mM isopropyl β-D-1-thiogalactopyranoside (IPTG) at 16°C for 16 hours in Terrific Broth. Cells were harvested and lysed using a microfluidizer. The lysate was clarified by centrifugation and then applied to a Ni-NTA (QIAGEN) column. Anion exchange (HiTrap Q HP, GE healthcare) chromatography was performed in a buffer of 50 mM Tris, pH 8.0 with a NaCl concentration gradient from 50 mM to 1M. Subsequent size exclusion chromatography (HiLoad Superdex 75, GE healthcare) was performed in a buffer of 50 mM Tris, 150 mM NaCl, pH 8.0. Purity of the proteins was analyzed by SDS-PAGE after each step. Full length eIF3j was expressed in *Escherichia coli* BL21 and purified with a similar method.

Filter binding assays

Rabbit 40S ribosome and binding partners (proteins or CrPV IRES RNA) were incubated together for 20 min at 37°C in a total volume of 20 μL in 1 × 48S buffer (20 mM HEPES(KOH) pH 7.5, 100 mM KCl, 2.5 mM MgAc, 1 mM DTT, 250 μM Spermidine 3HCl). Reaction mixtures were incubated for another 20 min at room temperature before diluting to 100 μL with H100 buffer (10 mM HEPES(KOH) pH 7.0, 100 mM KCl, 5 mM MgAc, 2 mM DTT). Diluted reaction mixtures were filtered through 100 kDa filter (Thermo Scientific) in 10,000 g for 5 min. The flow through was collected. 200 μL H100 buffer was used for washing the unbound proteins or RNA for 4 times before analyzing by SDS-PAGE or RNA gel.

The concentration for the 40S ribosome for the filter binding assay is 1.5 μM and the Nsp1 concentration is 15 μM (ratio of 1:10). In the Nsp1 and eIF3j competition assays, the concentrations of eIF3j are 7.5 μM, 15 μM and 30 μM corresponding to ratios of 1:5, 1:10 and 1:20. The concentration of the CrPV IRES is 7.5 μM in the Nsp1-IRES binding assay (ratio of 1:5).

Cryo-EM sample preparation, data collection and processing

40S ribosome and Nsp1, with or without the CrPV IRES RNA were mixed and incubated at 37°C for 20 mins to form a stable complex. The complex (4 μl) was applied to a C-Flat 2/1 3C copper grid (Electron Microscopy Sciences) pretreated by glow-discharging at 8 mA for 20 s. The grid was blotted at 20°C with 100% humidity and plunge-frozen in liquid ethane using FEI Vitrobot Mark IV (Thermo Fisher). The grids were stored in liquid nitrogen before data collection.

Images were acquired on a FEI Titan Krios electron microscope (Thermo Fisher) equipped with a post-GIF Gatan K3 direct detector in super-resolution mode, at a nominal calibrated magnification of 81,000 × with the physical pixel size corresponding to 1.068Å. Automated data collection was performed using SerialEM (Mastronarde, 2005).

A total of 4,700 movie series were collected for the Nsp1-40S ribosome complex. 300 movies series were collected for the Nsp1-40S-CrPV IRES complex. For the Nsp1-40S ribosome complex, a defocus range of 0.5 μm to 2 μm was used. Data were collected with a dose of 15.9 electrons per pixel per second. Images were recorded over a 3.6 s exposure with 0.1 s for each frame to give a total dose of 50 electrons per $Å^2$. Similar conditions were used for the Nsp1-40S-CrPV IRES complex.

The same data processing procedures were carried out for both the two complexes using standard pipelines in cryoSPARC(Punjani et al., 2017). The final average resolution is 2.7 Å for the Nsp1-40S ribosome complex and 3.3 Å for the Nsp1-40S-CrPV IRES complex (FSC = 0.143). Local refinement was carried out for the head domain of the 40S, which significantly increased the quality of the reconstruction for this domain (Figure S3D).

Model building and refinement

The structure of the rabbit 40S ribosome was extracted from PDB: 4KZX (Lomakin and Steitz, 2013) and 6SGC (Chandrasekaran et al., 2019). The model of Nsp1 C-terminal domain was manually built in COOT (Emsley et al., 2010). The CrPV IRES structure was extracted form PDB:5IT9 and refined (Murray et al., 2016). The structures of Nsp1-40S ribosome complex and Nsp1-IRES-40S ribosome complex were refined with phenix.real_space_refine module in PHENIX (Adams et al., 2010). All structural figures were generated using PyMol (Schrödinger, LLC, 2015) and Chimera (Pettersen et al., 2004).

QUANTIFICATION AND STATISTICAL ANALYSIS

Sample size determination

Sample size was determined according to the lab's prior work or similar approaches in the field.

Replication

All experiments were done with at least three biological replicates. Experimental replications were indicated in detail in methods section and in each figure panel's legend.

Standard statistical analysis

All statistical methods are described in figure legends and/or supplementary Excel tables. The P values and statistical significance were estimated for all analyses. For example, the unpaired, two-sided, t test was used to compare two groups. One-way ANOVA along with multiple comparisons test, was used to compare multiple groups. Multiple-testing correction was done using false discovery rate (FDR) method. Different levels of statistical significance were accessed based on specific p values and type I error cutoffs (0.05, 0.01, 0.001, 0.0001). Data analysis was performed using GraphPad Prism v.8. and/or RStudio.

Molecular Cell, Volume *80*

Supplemental Information

Nonstructural Protein 1 of SARS-CoV-2 Is a Potent Pathogenicity Factor Redirecting Host Protein Synthesis Machinery toward Viral RNA

Shuai Yuan, Lei Peng, Jonathan J. Park, Yingxia Hu, Swapnil C. Devarkar, Matthew B. Dong, Qi Shen, Shenping Wu, Sidi Chen, Ivan B. Lomakin, and Yong Xiong

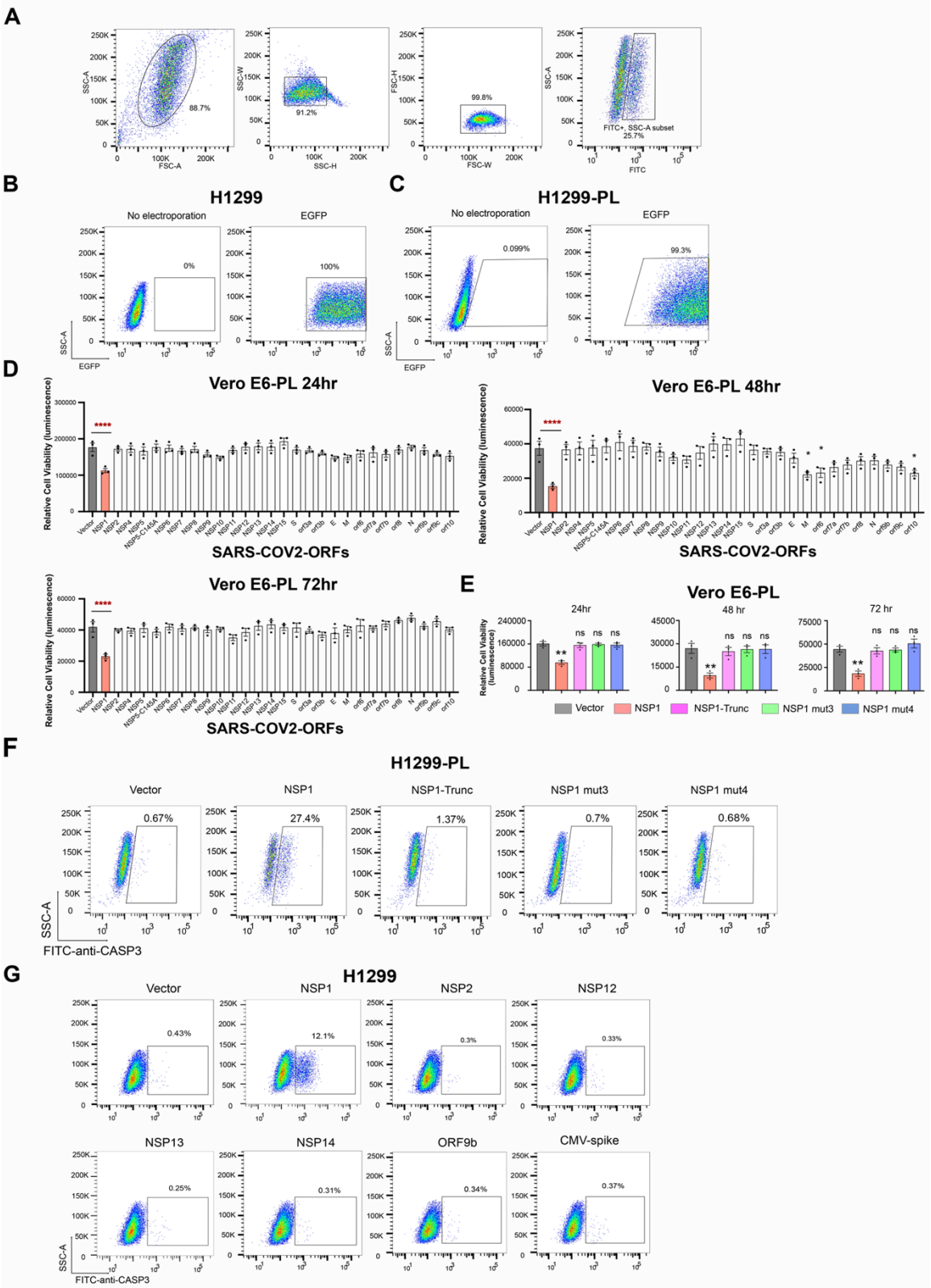

Figure S1. Flow cytometry analysis of cellular effects of SARS-CoV-2 ORFs, Nsp1, and Nsp1 mutants, Related to Figure 1.

(A) Diagram of example flow gating.
(B) Flow cytometry plots of GFP expression in H1299 cells, at 48 hours post ORF introduction.
(C) Flow cytometry plots of GFP expression in H1299-PL cells, at 48 hours post ORF introduction.
(D) Bar plot of firefly luciferase reporter measurement of viability effects of SARS-CoV-2 ORFs in Vero E6-PL cells, at 24, 48 and 72 hours post ORF introduction (n = 3 replicates).
(E) Bar plot of firefly luciferase reporter measurement of viability effects of Nsp1 and three Nsp1 mutants (truncation, mut3: R124S/K125E and mut4: N128S/K129E) in Vero E6-PL cells, at 24, 48 and 72 hours post ORF introduction (left, middle and right panels, respectively) (n = 3 replicates).
(F) Flow cytometry plots of apoptosis analysis of Nsp1 and three Nsp1 mutants (truncation, mut3: R124S/K125E and mut4: N128S/K129E) in H1299-PL cells, at 48 hours post ORF introduction. Percentage of apoptotic cells was gated as cleaved Caspase 3 positive cells.
(G) Flow cytometry plots of apoptosis analysis of several SARS-CoV-2 ORFs (Nsp1, Nsp2, Nsp12, Nsp13, Nsp14, Orf9b and Spike), at 48 hours post ORF introduction, in H1299 cells. Percentage of apoptotic cells was gated as cleaved Caspase 3 positive cells.

For all bar plots in this figure: Bar height represents mean value and error bars indicate standard error of the mean (sem). (n = 3 replicates for each group). Statistical significance was accessed by ordinary one-way ANOVA, with multiple group comparisons where each group was compared to empty vector control, with p-values subjected to multiple-testing correction by FDR method. (ns, not significant; * $p < 0.05$; ** $p < 0.01$; *** $p < 0.001$; **** $p < 0.0001$).

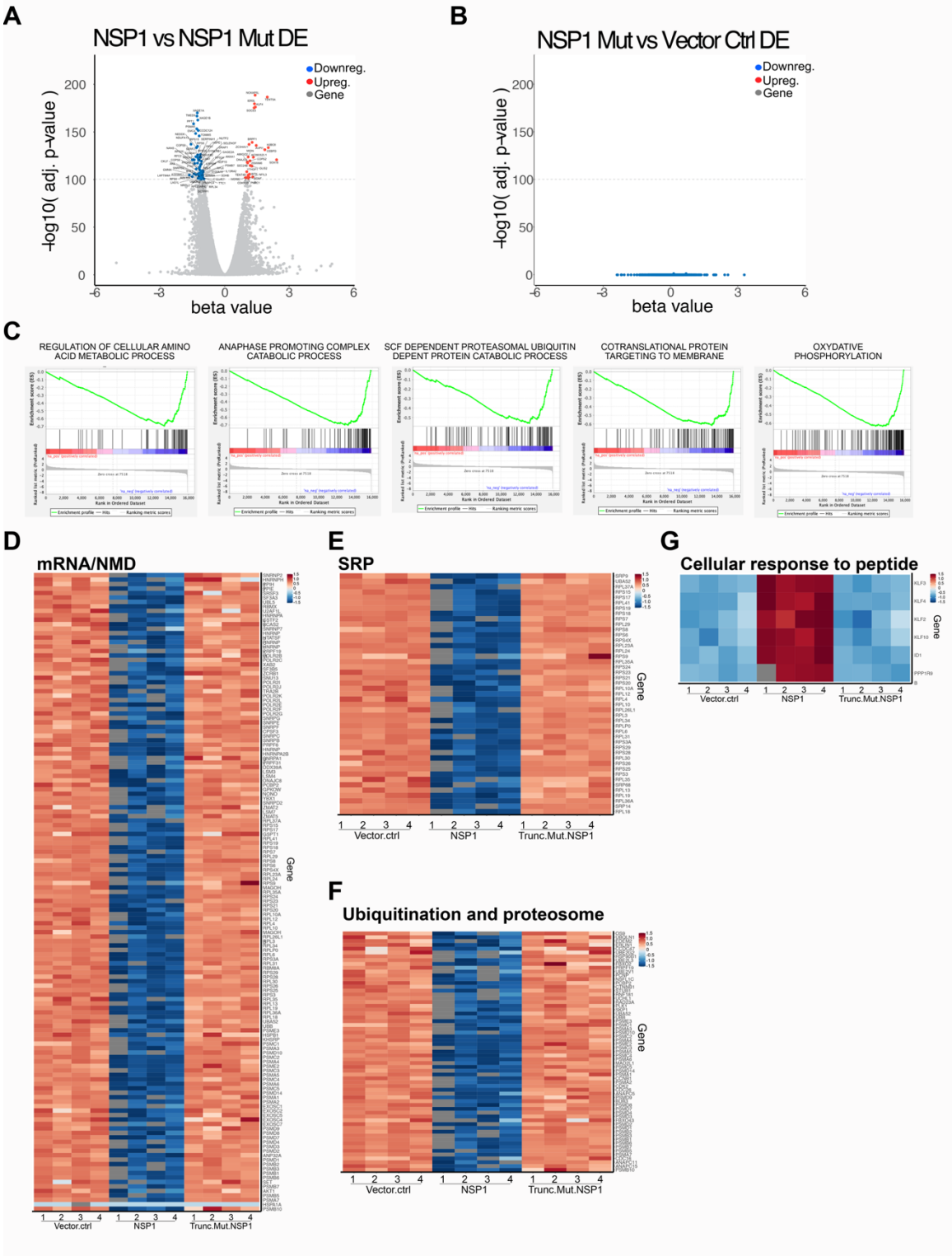

Figure S2. Additional differential expression and pathway analysis of H1299 Nsp1 mRNA-seq dataset, Related to Figures 2 and 3.

(A) Volcano plot of differential expression between of Nsp1 vs Nsp1 mutant electroporated cells. Genes highly differentially expressed (FDR adjusted

q value < 1e-100) are shown with gene names. Upregulated genes are shown in orange. Downregulated genes are shown in blue.

(B) Volcano plot of differential expression between of Nsp1 mutant vs Vector Control electroporated cells. As seen in the plot, no gene in the genome is differentially expressed between these two groups.

(C) Gene set enrichment plots of additional representative enriched pathways by GSEA.

(D) Heatmap of Nsp1 highly repressed genes (q < 1e-30) in the mRNA processing and nonsense-mediated decay processes.

(E) Heatmap of Nsp1 highly repressed genes (q < 1e-30) in the SRP proteins.

(F) Heatmap of Nsp1 highly repressed genes (q < 1e-30) in the ubiquitination and proteasome degradation processes.

(G) Heatmap of Nsp1 highly induced genes (q < 1e-30) in the cellular response to peptide processes.

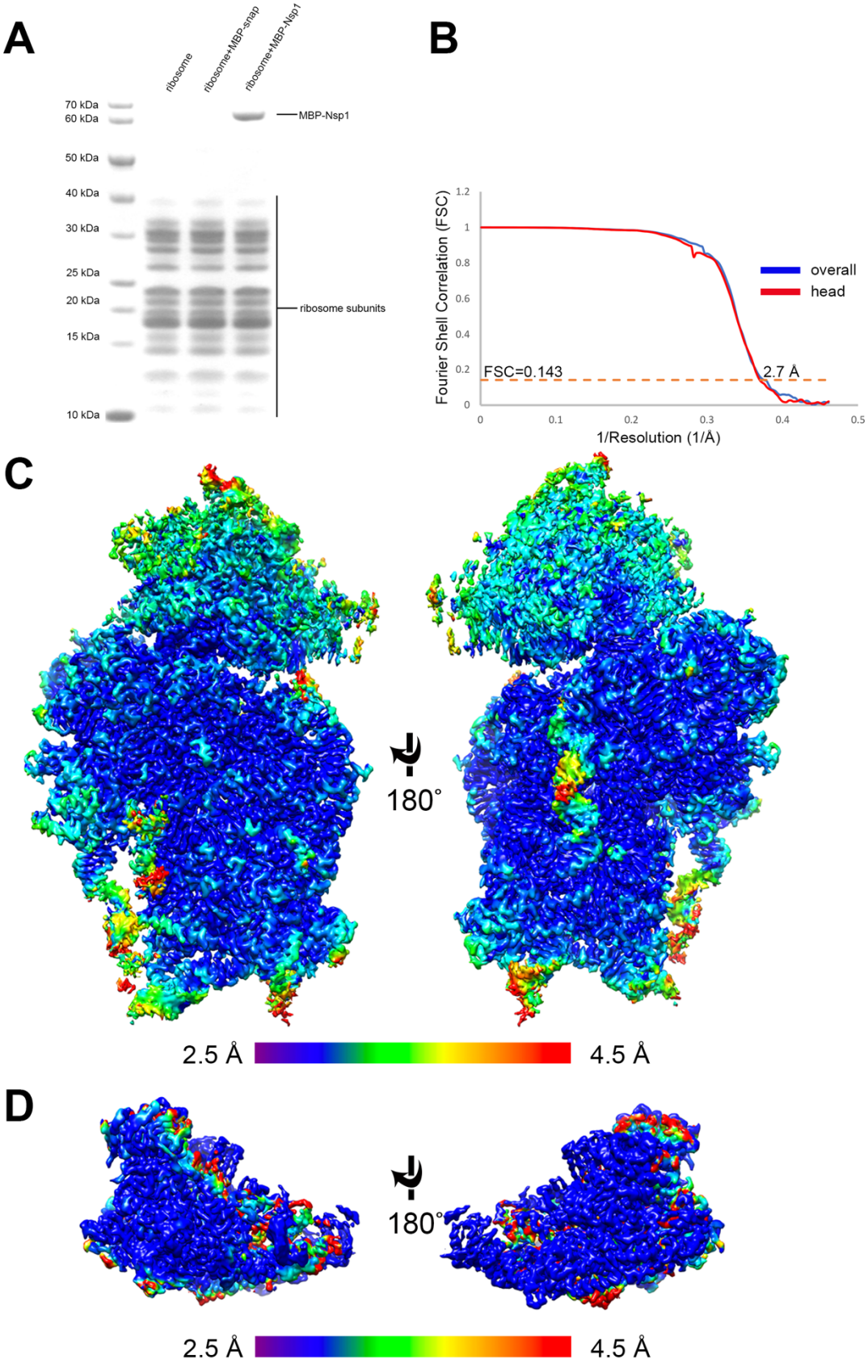
A
ribosome
ribosome+MBP-snap
ribosome+MBP-Nsp1
70 kDa
60 kDa
50 kDa
40 kDa
30 kDa
25 kDa
20 kDa
15 kDa
10 kDa
MBP-Nsp1
ribosome subunits
B
Fourier Shell Correlation (FSC)
1.2
1
0.8
0.6
0.4
0.2
0
0
0.1
0.2
0.3
0.4
0.5
1/Resolution (1/Å)
overall
head
FSC=0.143
2.7 Å
C
180°
2.5 Å
4.5 Å
D
180°
2.5 Å
4.5 Å

Figure S3. Data processing of Nsp1-40S ribosome complex cryo-EM dataset, Related to Figure 4.

(A) SDS-PAGE analysis of Nsp1 and 40S ribosome binding. Nsp1 is labeled with an MBP tag. MBP-snap was used as a negative control.

(B) FSC curves of the half-maps from gold standard refinement of the Nsp1-40S ribosome complex (blue) and masked local refinement of the head domain (red).

(C-D) Color coded local resolution estimation of the overall complex (**C**) and local-refined head domain (**D**).

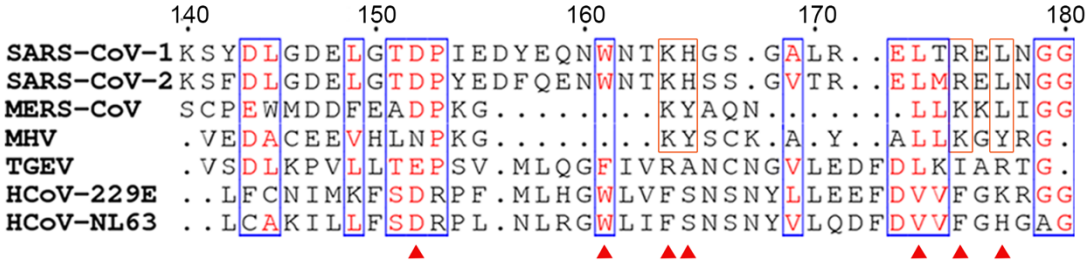

Figure S4. Alignment of the last 40 residues at Nsp1 C-terminus from beta-CoVs (SARS-CoV, SARS-CoV-2, MERS-CoV and MHV) and alpha-CoVs (TGEV, HCoV-229E and HCoV-NL63), Related to Figure 4.

Residues conserved in both alpha- and beta-CoVs are boxed in blue. Residues only conserved in beta-CoVs are with orange boxes. Conserved residues that mediate the interaction with the 40S are marked with red triangles.

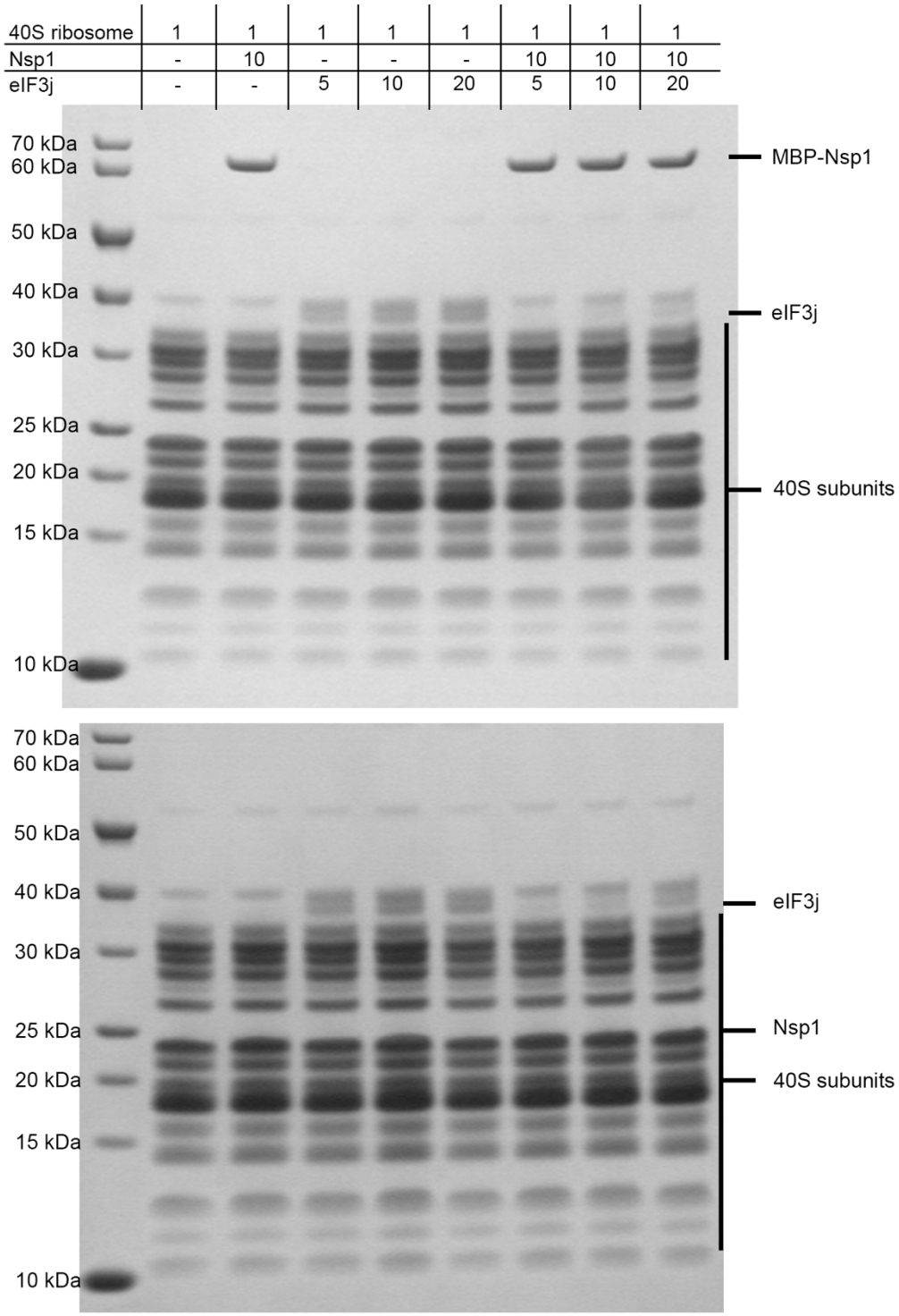

Figure S5. SDS-PAGE analysis of Nsp1 and eIF3j competition assay, Related to Figure 4.

Concentration ratios are shown in top table. Top gel: Assay with MBP-Nsp1. Bottom gel: Full-length Nsp1 without the MBP tag was used to exclude the tag effect.

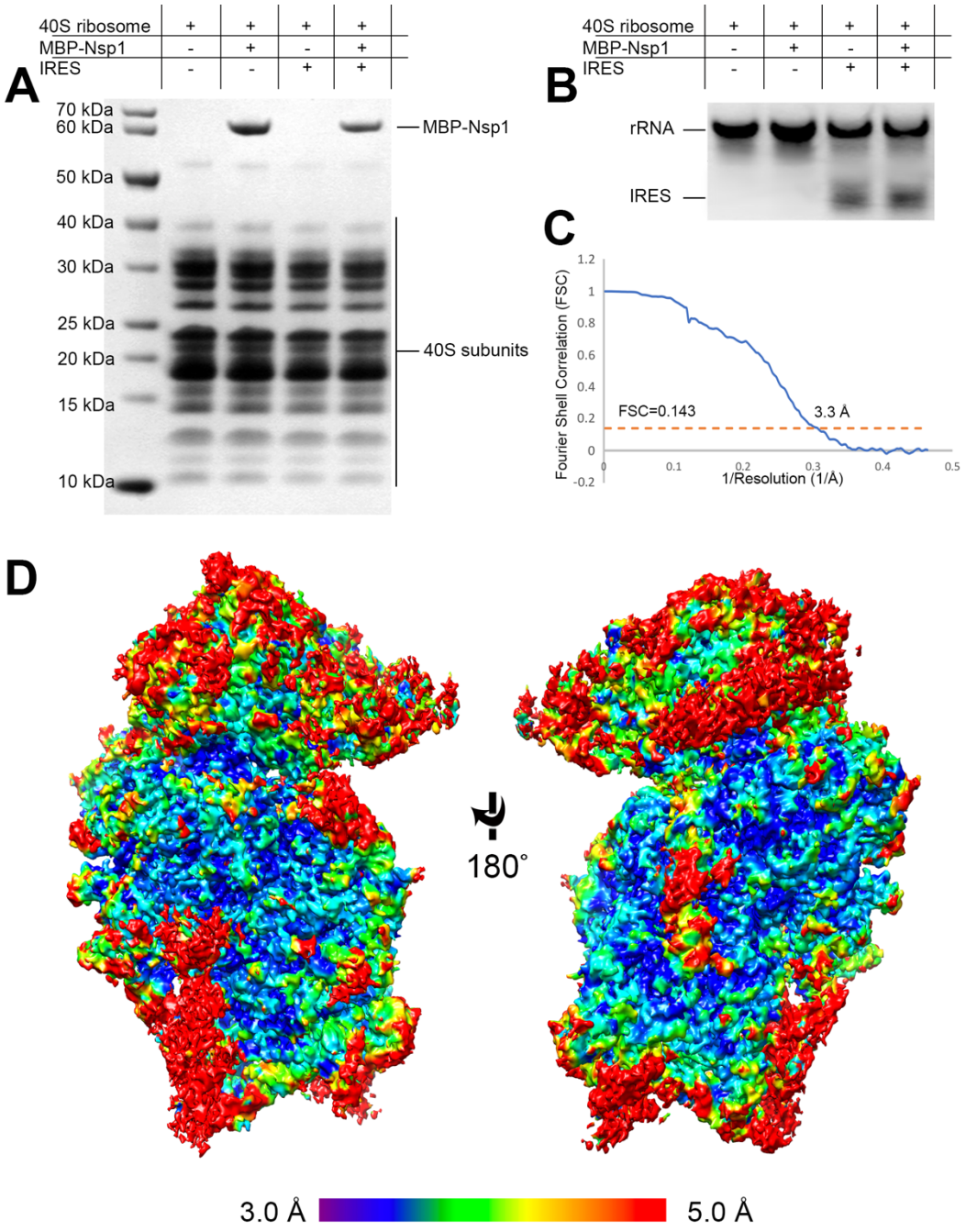

Figure S6. Data processing of Nsp1-40S-CrPV IRES complex cryo-EM dataset, Related to Figure 5.

(A-B) CrPV IRES and Nsp1 can bind to 40S ribosome simultaneously. SDS-PAGE. analysis **(A)** and RNA gel analysis **(B)** show the binding of Nsp1 and CrPV IRES.

(C) FSC curves of the half-maps from gold standard refinement of the Nsp1-40S-CrPV IRES complex.

(D) Color coded local resolution estimation of the complex.